A Letter of Intent to The J-PARC 50-GeV Proton Synchrotron Experiment

An Experimental Search for the $\mu^- - e^-$ Conversion Process at an Ultimate Sensitivity of the Order of 10^{-18} with PRISM

The PRIME Working Group

January 1, 2003

The PRIME (PRISM Mu E) Working Group Members

Shinji Machida, Yoshiharu Mori*, Chihiro Ohmori, and Takeichiro Yokoi
Accelerator Laboratory, High Energy Accelerator Research Organization (KEK),

Tatsushi Nakamoto, Toru Ogitsu, and Akira Yamamoto
Cryogenics Science Center, High Energy Accelerator Research Organization (KEK),

Yoichi Igarashi, Shigeru Ishimoto and Koji Yoshimura*
Institute of Particle and Nuclear Studies, High Energy Accelerator Research Organization (KEK),

Noboru Sasao*
Department of Physics, Kyoto University,

Yoshihisa Iwashita
Institute for Chemical Research, Kyoto University,

Hiroyuki Ohnishi
Graduate School of Engineering, Kyushu University,

Masaharu Aoki, Yoshitaka Kuno*, Fumitaka Maeda, Kengo Nakahara, Norihito Nosaka, Akira Sato, and Yosuke Takubo
Department of Physics, Graduate School of Science, Osaka University.

The * mark indicates the contact persons.

Abstract

We, the PRIME (PRISM Mu E conversion) working group, would like to express our interest to carry out a search for a lepton-flavor-violating $\mu^- - e^-$ conversion process in a muonic atom at an ultimate sensitivity of the order of 10^{-18} by using a proposed high intensity muon source called PRISM. PRISM stands for `Phase Rotated Intense Slow Muon source`. It would provide a muon beam of the world-highest brightness of about $10^{11} - 10^{12} \mu^{\pm}$/sec with narrow momentum width and small pion contamination in a beam.

The major advantages of the use of the PRISM beam are (1) to allow us to use a very thin muon-stopping target so as to make the energy resolution of electron detection better, (2) to eliminate pion contamination that is a serious background for the search, and (3) to reduce a cosmic-ray background. The aimed sensitivity is sufficient enough to cover most of theoretical predictions such as supersymmetric grand-unification (SUSY-GUT) and the minimal supersymmetric standard model, a model of extra-dimension. The discovery potential is very high. It would, if discovered, indicate a clear signal of physics beyond the Standard Model.

Contents

Chapter 1

Executive Summary

Physics Motivation of Lepton Flavor Violation : Lepton flavor violation (LFV) attracts much interest from theorists and experimentalists since it has a large discovery potential to find a clue of new physics beyond the Standard Model, in particular supersymmetric extension to the Standard Model. The LFV processes are sensitive to supersymmetric grand unification models (SUSY-GUT), either SU(5) or SO(10), minimal supersymmetric standard models with right-handed Majorana neutrinos, a model of extra-dimension, and so on.

Among many systems to study LFV, the muon is superb since a number of muons available is the most, much larger than a number of taus. The number of muons available at present is an order of 10^{15} muons/year, and we anticipate more, with a new high intensity muon source called PRISM, like $10^{18} - 10^{19}$ muons/year. On the contrary, a number of taus is about 10^7/year at present, and will become about 10^9/year at even a super B factory.

Among many muon LFV processes, we think, the $\mu^-{-}e^-$ conversion process is the best, since the other process such as $\mu^+ \rightarrow e^+\gamma$ will be limited by accidental backgrounds. Unless detection resolutions are improved by new detector technology (especially for photon detection), it would be difficult to go beyond the sensitivity of 10^{-14}, which is the goal of the present PSI experiment. However, in the $\mu^-{-}e^-$ conversion process, the detector resolution is not a critical issue. **The most important is a muon beam with good quality and no contamination**. If a good muon beam is constructed, a sensitivity will be improved by availability of more muons. This has motivated us to construct a new high intensity muon source with narrow energy spread and no pion contamination in a beam.

PRISM : PRISM is a project to construct a dedicated source of a high intensity muon beam with narrow energy spread and small beam contamination. PRISM stands for "`Phase Rotated Intense Slow Muon source`". The aimed muon beam intensity is about $10^{11} - 10^{12}$ $\mu^{\pm}$/sec, four orders of magnitude higher than that available at present. The narrow beam energy spread can be achieved by a novel technique of phase rotation, which accelerates slow muons and decelerates fast muons by a radio frequency (RF) field. Small beam contamination, in particular a pion contamination of the level of 10^{-18}, can be achieved by a long flight length of a beam so that most of pions decay out.

PRIME : PRIME (PRISM Mu E conversion) is an experiment to search for $\mu^- - e^-$ conversion at an ultimate sensitivity of $B(\mu^- + A \rightarrow e^- + A) < 10^{-18}$ with a muon beam from PRISM. That sensitivity would cover most of the parameter space available in SUSY-GUT. The advantages of PRIME are to have (1) a high sensitivity due to high muon intensity, and (2) low background rates. In particular, the second would allow us a multiple-year running to achieve the sensitivity. In addition to studies of PRISM itself, spectrometer options and detector R&D have been already started. The experimental strategy will depend on funding situation, technology available, and the situation of the other LFV experiments.

The discovery potential for PRIME is very high. If a $\mu^- - e^-$ conversion processes is found with PRIME, this would indicate a clear signal of physics beyond the Standard Model.

Chapter 2

Physics Motivation

2.1 Why Do We Search For Lepton Flavor Violation in the Muon ?

Recently, lepton flavor violation (LFV) has attracted much interest from theorists and experimentalists in particle physics, since it has a growing potential to find an important clue of new physics beyond the Standard Model, such as supersymmetric extension to the Standard Model [1]. Some of the notable features on the LFV studies are that (1) LFV might have sizable contributions from new physics, which could be observable in future experiments, and that (2) LFV does not have any sizable Standard Model contribution, which could become serious background otherwise.

The muon system is one of the best places to search for LFV [1]. Historically the search for LFV has been initiated by Hincks and Pontecorvo in 1947 [2]. Since then, the upper limits have been improved at a rate of two orders of magnitude per decade, as seen in Fig. 2.1. In Table 2.1, the upper limits of various LFV decays are listed. From Table 2.1, it is seen that the sensitivity to LFV is superb in the muon system. It is mostly because of a large number of muons available for experimental searches today (of about $10^{14} - 10^{15}$/year). And a number of muons available would become more in future if a new highly intense muon source (such as PRISM) is realized.

2.2 Theoretical Predictions

In the minimal Standard Model, lepton flavor conservation is built in by hand with assuming vanishing neutrino masses. As a matter of fact, any new physics or interaction beyond the Standard Model would predict LFV at some level. Among various theoretical models, two scenarios based on supersymmetric models are briefly presented as follows.

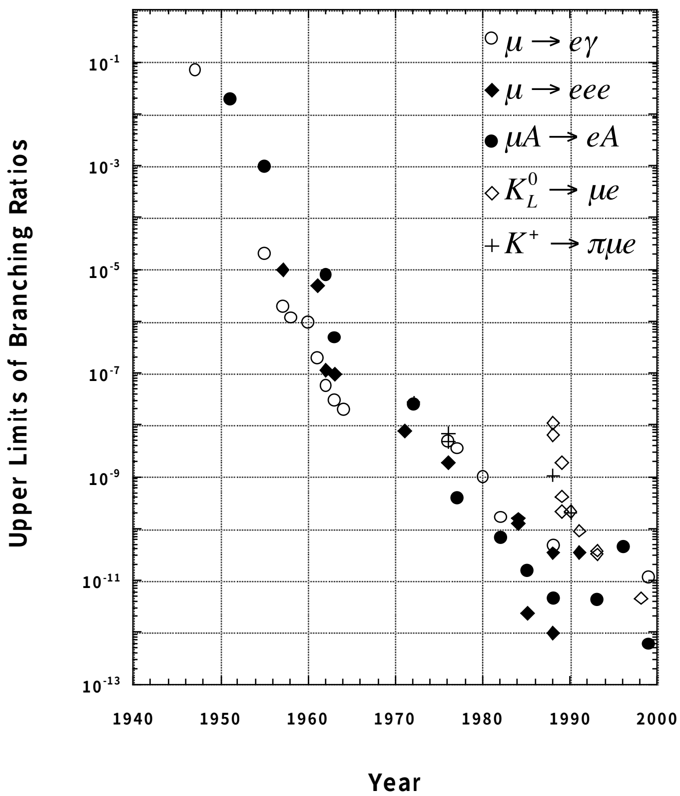

Figure 2.1: History of searches for LFV in muon and kaon decays

2.2.1 Supersymmetric Grand Unified Theory (SUSY-GUT)

Supersymmetric (SUSY) extension to the Standard Model, in particular supersymmetric grand unified theories (SUSY-GUT), has attracted considerable interest regarding LFV processes. In SUSY-GUT, finite slepton mixing appears unavoidably through radiative corrections in the renormalization group evolution from the GUT

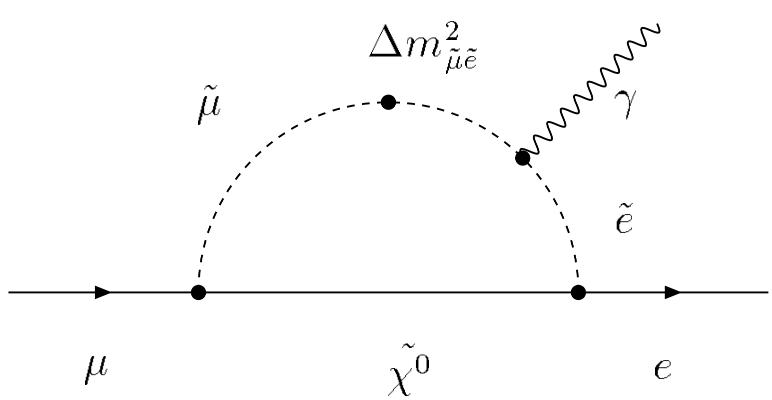

Figure 2.2: Typical diagram of $\mu^+ \to e^+\gamma$ in SU(5) SUSY models.

Table 2.1: Limits of the lepton-flavor violating decays of muon, tau, pion, kaon and Z boson.

Reaction	Present limit	Reference
$\mu^+ \to e^+\gamma$	$< 1.2 \times 10^{-11}$	[3]
$\mu^+ \to e^+e^+e^-$	$< 1.0 \times 10^{-12}$	[4]
$\mu^- Ti \to e^- Ti$	$< 6.1 \times 10^{-13}$	[5]
$\mu^+e^- \to \mu^-e^+$	$< 8.3 \times 10^{-11}$	[6]
$\tau \to e\gamma$	$< 2.7 \times 10^{-6}$	[7]
$\tau \to \mu\gamma$	$< 3.0 \times 10^{-6}$	[7]
$\tau \to \mu\mu\mu$	$< 1.9 \times 10^{-6}$	[8]
$\tau \to eee$	$< 2.9 \times 10^{-6}$	[8]
$\pi^0 \to \mu e$	$< 8.6 \times 10^{-9}$	[9]
$K_L^0 \to \mu e$	$< 4.7 \times 10^{-12}$	[10]
$K^+ \to \pi^+\mu^+e^-$	$< 2.1 \times 10^{-10}$	[11]
$K_L^0 \to \pi^0\mu^+e^-$	$< 3.1 \times 10^{-9}$	[12]
$Z^0 \to \mu e$	$< 1.7 \times 10^{-6}$	[13]
$Z^0 \to \tau e$	$< 9.8 \times 10^{-6}$	[13]
$Z^0 \to \tau\mu$	$< 1.2 \times 10^{-5}$	[14]

scale to the weak energy scale, even if the diagonal slepton mass matrix is assumed at the Planck scale [15]. Recently, it was pointed out that the slepton mixing thus generated is very large owing to the large top-quark Yukawa coupling [16]. Then, $\mu^+ \to e^+\gamma$ occurs through this slepton mixing through the loop diagram shown in Fig. 2.2. The branching ratios of $\mu^+ \to e^+\gamma$ predicted in SUSY SU(5) models [1] are shown in Fig. 2.3. They range from 10^{-15} to 10^{-13} for the singlet smuon mass of $m_{\tilde{\mu}_R}$ of 100 to 300 GeV [17]. They are larger for a large $\tan\beta$ value. The SO(10) SUSY GUT models give an even larger value of 10^{-13} to 10^{-11} by an enhancement of $(m_\tau^2/m_\mu^2) \sim 100$ [16]. It is because of the existence of loop diagrams whose magnitude is proportional to the tau-lepton mass in SO(10) SUSY-GUT models. The predicted branching ratio of $\mu^+ \to e^+\gamma$ in SUSY SO(10) models are shown in Fig. 2.4 [1].

2.2.2 Supersymmetric Models with Right-handed Neutrinos

The other model is supersymmetric models with right-handed neutrinos. As widely known, there is considerable evidence for the existence of neutrino masses and their mixing. In the SUSY model with right-handed Majonara neutrinos, the slepton mixing can be induced from the neutrino mixing. Then, LFV processes in muon decays are also expected to occur [18, 19, 20]. There are two possible contributions to the slepton mixing between $\tilde{\mu}$ and $\tilde{e}$. One is from V_{21} (between ν_1 and ν_2), corresponding to the solar neutrino mixing. The other is from the product of V_{31} (between ν_3 and ν_1) and V_{32} (between ν_3 and ν_2) that corresponds to the atmospheric neutrino mixing.

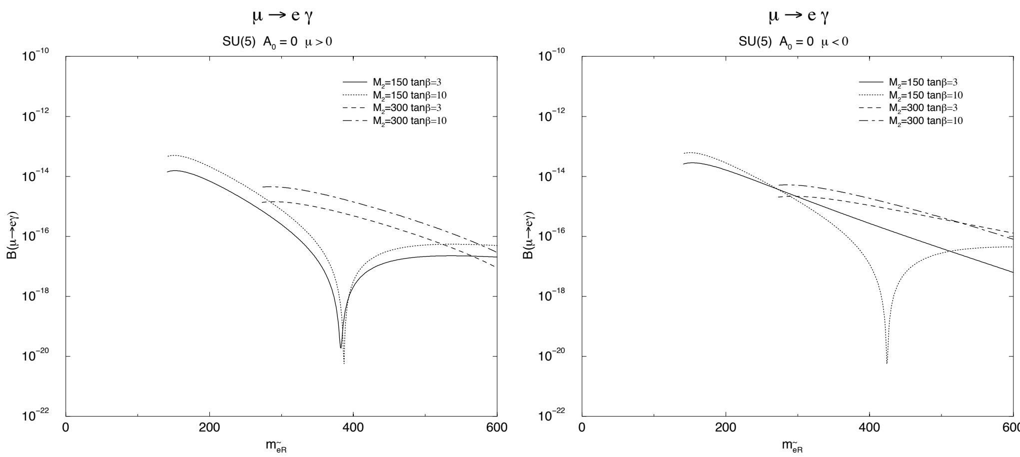

Figure 2.3: Predictions of $\mu^+ \to e^+\gamma$ branching ratio in SU(5) SUSY models. (a) is $\mu > 0$ and (b) is $\mu < 0$, where μ is one of the SUSY parameters.

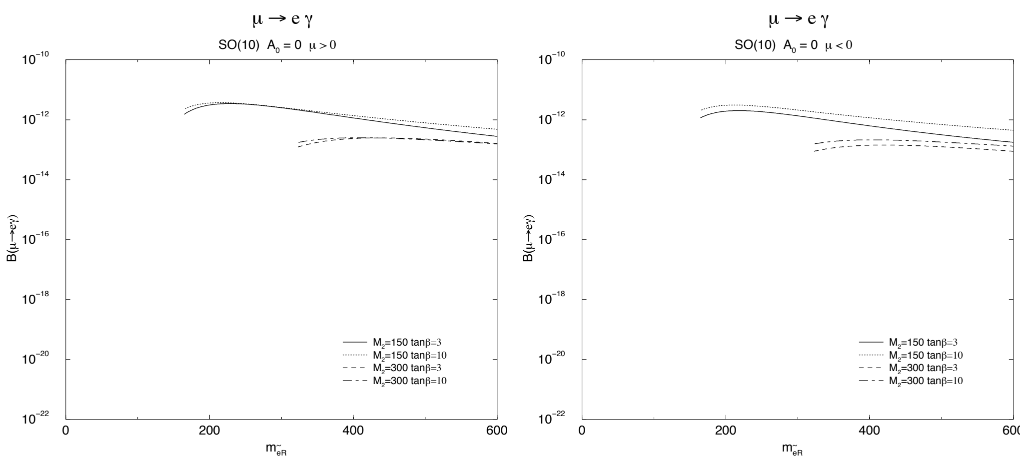

Figure 2.4: Predicted branching ratios for $\mu^+ \to e^+\gamma$ decay in the $SO(10)$ SUSY GUT based on the minimal supergravity model.

Here, ν_i $(i = 1-3)$ are the mass eigenstates of neutrinos. Since V_{31} is not known, the second contribution can not be estimated. The former contribution, however, can be estimated by the information from the solar neutrino and KamLAND data. There were several allowed regions for the solar neutrino mixing: the MSW large-angle solution (LMA), the MSW small-angle solution (SMA) and the vacuum oscillation (VO), as shown in the left plot in Fig. 2.5. Recently, the LMA solution is confined by the KamLAND experiment. Take the V_{21} value thus obtained, the predictions for $\mu^+ \to e^+\gamma$ are shown as a function of the mass of the heavy right-handed Majorana neutrino mass ν_{R2} $(m_{\nu_{R2}})$ in the right plot in Fig. 2.5. As seen, the predictions are as large as the present experimental limit or even larger.

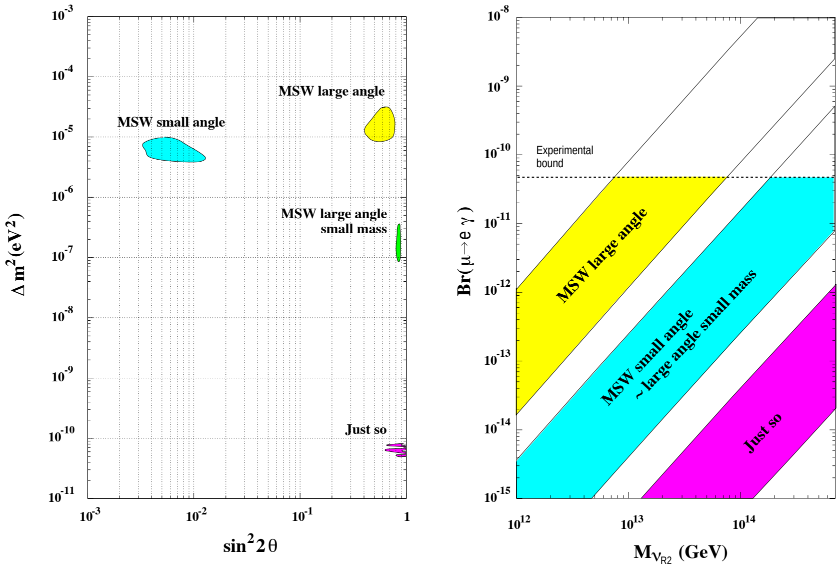

Figure 2.5: Predictions of $\mu^+ \to e^+\gamma$ branching ratio in MSSM with right-handed neutrino. (left) the MSW large mixing angle, and (right) the MSW small mixing angle. The recent KamLAND experiment confined that the LMA solution is correct. The experimental bound is from the Particle Data Group, although a new limit of 1.2×10^{-11} is reported recently from MEGA.

2.2.3 $\mu^-{-}e^-$ conversion and $\mu^+ \to e^+\gamma$

As explained later, there could be two contributions in the $\mu^-{-}e^-$ diagrams. One is a photonic contribution, and the other is a non-photonic contribution. For the photonic contribution, there is some relation between the $\mu^-{-}e^-$ conversion process and the $\mu^+ \to e^+\gamma$ decay. Suppose a photonic contribution is dominant, the branching ratio of the $\mu^- - e^-$ conversion process is expected be smaller than that of $\mu^-{-}e^-$ decay by a factor of α, namely about a few hundred. It implies that the search for $\mu^-{-}e^-$ conversion at the level of 10^{-16} is comparable to that for $\mu^+ \to e^+\gamma$ at the level of 10^{-14}.

More precisely, this factor depends on the nucleus used in the $\mu^-{-}e^-$ conversion search [21]. For instance, the factor in Ti is about 1/250 the branching ratio of $\mu^+ \to e^+\gamma$. With taking account of relativistic atomic effects, Coulomb distortion, finite nuclear size and nucleon distribution, it was found that the ratio of $\mu^-{-}e^-$ conversion to $\mu^+ \to e^+\gamma$ varies from 1/389 for ^{27}Al to 1/238 for ^{48}Ti, and decreases again to 1/342 for ^{208}Pb [22].

If the non-photonic contribution dominates, there is no relation between $\mu^+ \to e^+\gamma$ decay and $\mu^-{-}e^-$ conversion. It would be worth to note the following. When a $\mu^+ \to e^+\gamma$ signal is found, then a $\mu^-{-}e^-$ conversion signal has to be found. When no $\mu^+ \to e^+\gamma$ signal is found, there is still opportunity to find a $\mu^-{-}e^-$ conversion signal if non-photonic contribution exits.

Regarding the non-photonic contribution, it is argued that an extra logarithmic enhancement of the photonic loop diagrams for $\mu^- - e^-$ conversion (and also $\mu^+ \rightarrow e^+e^-e^+$) over $\mu^+ \rightarrow e^+\gamma$ has also been discussed [23]. It happens only when light charged fermions, to which a photon is attached, are involved in the loop diagrams. Therefore, it could occur for SUSY models with R-parity breaking, but not for R-parity conserving SUSY models or SUSY-GUT models.

Chapter 3

Phenomenology of $\mu^- - e^-$ Conversion Process

3.1 What is The $\mu^- - e^-$ Conversion Process ?

One of the prominent muon LFV process is $\mu^- - e^-$ conversion in a muonic atom. When a negative muon is stopped in some material, it is trapped by an atom, and forms a muonic atom. After it cascades down in energy levels in the muonic atom, a muon is bound in its $1s$ ground state. The fate of the muon is then either decay in an orbit ($\mu^- \to e^- \nu_\mu \overline{\nu}_e$) or capture by a nucleus of mass number A and atomic number Z, namely

$$\mu^- + (A, Z) \to \nu_\mu + (A, Z - 1). \tag{3.1}$$

However, in the context of physics beyond the Standard Model, the exotic process of neutrinoless muon capture, such as

$$\mu^- + (A, Z) \to e^- + (A, Z), \tag{3.2}$$

is also expected. This process is called $\mu^- - e^-$ conversion in a muonic atom. It violates the conservation of the lepton flavor numbers, L_e and L_μ, by one unit, but conserves the total lepton number, L.

The branching ratio of $\mu^- - e^-$ conversion can be given by

$$B(\mu^- + (A, Z) \to e^- + (A, Z)) \equiv \frac{\Gamma(\mu^- + (A, Z) \to e^- + (A, Z))}{\Gamma(\mu^- + (A, Z) \to capture)}, \tag{3.3}$$

where Γ is the corresponding decay width.

The final state of the nucleus (A, Z) could be either the ground state or excited states. In general, the transition process to the ground state, which is called coherent capture, is dominant. The rate of the coherent capture process over non-coherent ones is enhanced by a factor approximately equal to the number of nucleons in the nucleus, since all of the nucleons participate in the process.

3.1.1 Event Signature

The event signature of the coherent $\mu^-{-}e^-$ conversion in a muonic atom is a mono-energetic single electron emitted from the conversion with an energy of

$$\begin{aligned} E_{\mu e} &= m_\mu - B_\mu - E^0_{rec} \\ &\approx m_\mu - B_\mu, \end{aligned} \tag{3.4}$$

where m_μ is the muon mass, and B_μ and E^0_{rec} are the binding energy of the 1s muonic atom and the nuclear-recoil energy respectively. The nuclear-recoil energy is approximately $E^0_{rec} \approx (m_\mu - B_\mu)^2/(2M_A)$, where M_A is the mass of the recoiling nucleus, which is small. Since B_μ is different for various nuclei, the peak energy of the $\mu^-{-}e^-$ conversion signal changes. For instance, it varies from $E_{\mu e} = 104.3$ MeV for titanium to $E_{\mu e} = 94.9$ MeV for lead.

From an experimental point of view, $\mu^-{-}e^-$ conversion is very attractive. Firstly, the e^- energy of about 105 MeV is far above the end-point energy of the muon decay spectrum ($\sim$ 52.8 MeV). Secondly, since the event signature is a mono-energetic electron, no coincidence measurement is required. The search for this process has the potential to improve the sensitivity by using a high muon rate without suffering from accidental background, which would be serious backgrounds for other processes, such as $\mu^+ \to e^+\gamma$ and $\mu^+ \to e^+e^+e^-$ decays.

3.2 Theoretical Framework

The possible contributions to $\mu^-{-}e^-$ conversion in a muonic atom can be grouped into two parts, which are the photonic contribution and the non-photonic contribution. In principle, this process is theoretically more interesting than $\mu^+ \to e^+\gamma$, since **it does occur by mechanisms which do not contribute to the $\mu^+ \to e^+\gamma$ process**. The study of the photonic contribution was initiated by Weinberg and Feinberg [24]. The non-photonic contribution was studied later, for instance by [25].

The most general LFV interaction Lagrangian which contributes to the $\mu - e$ transition is given by [25]

$$\begin{aligned} \mathcal{L} = & -\frac{4G_F}{\sqrt{2}}(m_\mu A_R \bar{\mu}\sigma^{\mu\nu}P_L e F_{\mu\nu} + m_\mu A_L \bar{\mu}\sigma^{\mu\nu}P_R e F_{\mu\nu} + h.c.) \\ & -\frac{G_F}{\sqrt{2}}\sum_{q=u,d,s}[(g_{LS(q)}\bar{e}P_R\mu + g_{RS(q)}\bar{e}P_L\mu)\bar{q}q \\ & \qquad + (g_{LP(q)}\bar{e}P_R\mu + g_{RP(q)}\bar{e}P_L\mu)\bar{q}\gamma_5 q \\ & \qquad + (g_{LV(q)}\bar{e}\gamma^\mu P_L\mu + g_{RV(q)}\bar{e}\gamma^\mu P_R\mu)\bar{q}\gamma_\mu q \\ & \qquad + (g_{LA(q)}\bar{e}\gamma^\mu P_L\mu + g_{RA(q)}\bar{e}\gamma^\mu P_R\mu)\bar{q}\gamma_\mu\gamma_5 q \\ & \qquad + \frac{1}{2}(g_{LT(q)}\bar{e}\sigma^{\mu\nu}P_R\mu + g_{RT(q)}\bar{e}\sigma^{\mu\nu}P_L\mu)\bar{q}\sigma_{\mu\nu}q + h.c.], \end{aligned} \tag{3.5}$$

where G_F and m_μ are the Fermi constant and the muon mass, respectively, and $A_{L,R}$ and g's are all dimensionless coupling constants for the corresponding operators. The conventions used here are $F_{\mu\nu} = \partial_\mu A_\nu - \partial_\nu A_\mu$, $\sigma^{\mu\nu} = (i/2)[\gamma^\mu, \gamma^\nu]$, $P_L = (1-\gamma_5)/2$, $P_R = (1+\gamma_5)/2$, and the covariant derivative is defined as $D_\mu = \partial_\mu - iQeA_\mu$, where $Qe(e > 0)$ is the electric charge ($Q = -1$ for the electron and muon).

3.2.1 Nuclear Dependence

To study the nuclear dependence, detail calculations on the $\mu^-{-}e^-$ conversion rates have to be made. The initial state is the $1s$ state of the muonic atom and the final state is an out-going electron with the energy of $m_\mu - B_\mu$. Both wave functions have to be relativistic. Then, the conversion rate is given by the matrix element based on the Lagrangian in Eq.(3.5), where has to be integrated with the initial muon wave function and the final out-going electron wave function. The overlap integrals are calculated by Kitanno *et al.* [26]. They are given as follows.

$$\begin{aligned}\Gamma(\mu^- A \to e^- A) &= 2G_F^2 |A_R^* D + \tilde{g}_{LS}^{(p)} S^{(p)} + \tilde{g}_{LS}^{(n)} S^{(n)} + \tilde{g}_{LV}^{(p)} V^{(p)} + \tilde{g}_{LV}^{(n)} V^{(n)}|^2 \\ &+ 2G_F^2 |A_L^* D + \tilde{g}_{RS}^{(p)} S^{(p)} + \tilde{g}_{RS}^{(n)} S^{(n)} + \tilde{g}_{RV}^{(p)} V^{(p)} + \tilde{g}_{RV}^{(n)} V^{(n)}|^2, \quad (3.6)\end{aligned}$$

where $\tilde{g}$ are coupling constants and D, S and V are the overlap integrals, which are defined in Ref.[26]. They have three components, which are the photonic dipole operators (A_L and A_R), the scalar operators (g_{LS} and g_{RS}), and the vector operators (g_{LV} and g_{RV}). The dipole operators appear as a good approximation in SUSY models, especially in SO(10) SUSY GUT models and in SUSY with right-handed neutrinos. The scalar operators appear in SUSY models with R-parity violations, and the vector operators appear in the monopole $\mu - e - \gamma$ transition.

To calculate the overlap integrals, the proton and neutron distributions have to be known. The proton distribution is known by electron scattering precisely, however, the neutron distribution is only poorly known. Kitanno *et al.* [26] studied several cases, which are (method 1) the neutron distribution equal to the proton distribution, (method 2) the neutron distribution obtained from the pionic atom measurements, where the distribution is given by the two-parameter Fermi function, and (method 3) the neutron distribution from the polarized proton scattering experiments, where the data are available only for carbon, titanium, nickel, zirconium, and lead. Among the three, (method 3) gives the most reliable results. The $\mu^-{-}e^-$ conversion ratios (which is normalized by that in aluminum) is shown in Fig.3.1, 3.2 and 3.3 by the (method 1), (method 2), and (method 3), respectively. All of the three plots show similar tendency on the nuclear dependence. Namely, the $\mu^-{-}e^-$ conversion ratio increases as Z for $Z \leq 30$, are largest for $30 \leq Z \leq 60$, and decreases for $Z \geq 60$. It is also seen that the conversion ratios have large differences in heavy nuclei, depending on the three types of interaction. From this property we may be able to distinguish models beyond the Standard Model through several experiments with different targets.

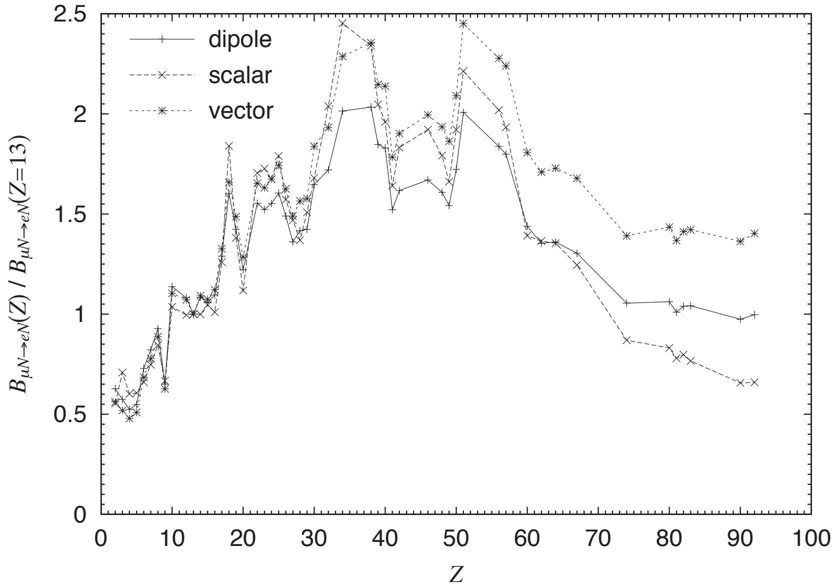

Figure 3.1: The $\mu^- - e^-$ conversion ratios calculated by (method 1) as a function of the atomic number Z. The solid, long-dashed, and dashed lines represent the case of the photonic dipole, scalar, and vector operators respectively.

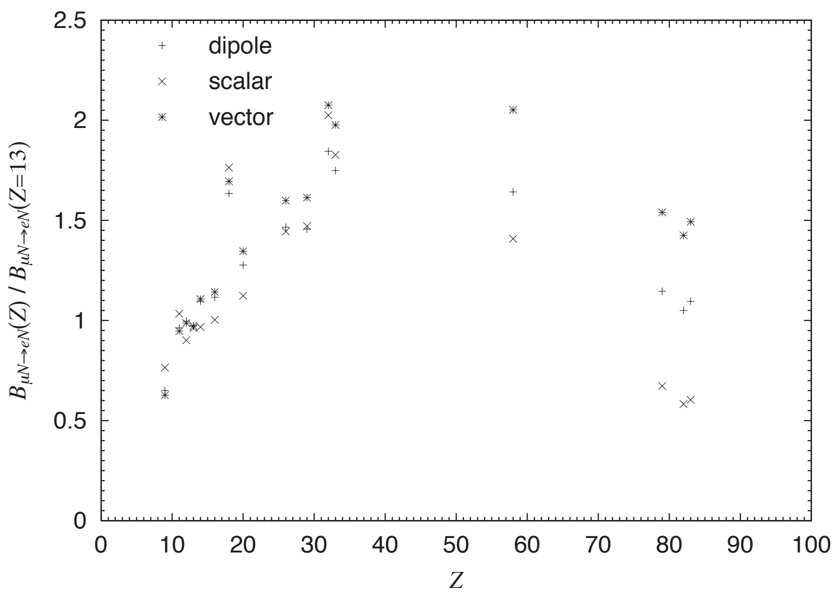

Figure 3.2: The $\mu^- - e^-$ conversion ratios calculated by (method 2) as a function of the atomic number Z. The marks of "+", "×", and "*" represent the case of the photonic dipole, scalar, and vector operators respectively.

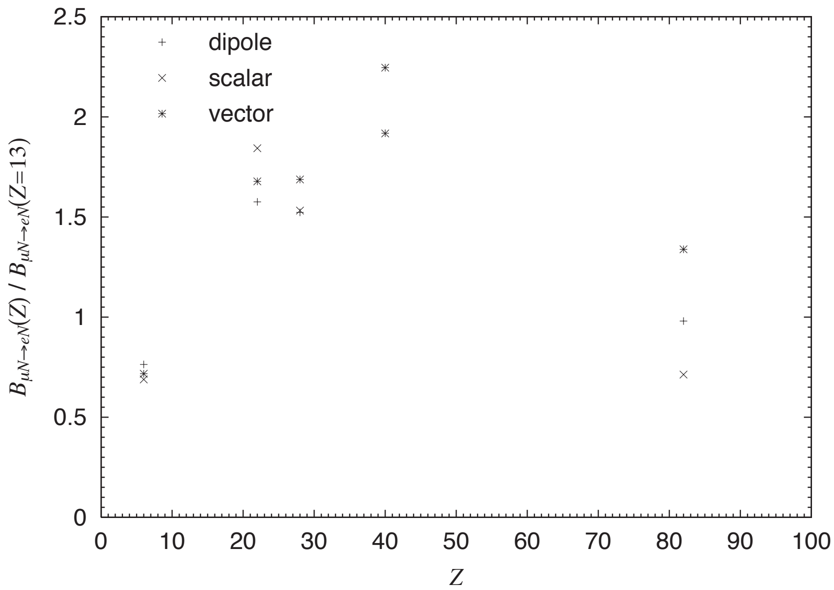

Figure 3.3: The $\mu^-{-}e^-$ conversion ratios calculated by (method 3) as a function of the atomic number Z. The marks of "+", "×", and "*" represent the case of the photonic dipole, scalar, and vector operators respectively.

3.3 Present Status of the Searches

In this subsection, the present status of the LFV experiments with muons in particular, the searches for $\mu^-{-}e^-$ conversion and$\mu^+ \to e^+\gamma$ decay are presented.

3.3.1 Experimental status of $\mu^-{-}e^-$ conversion

Table 3.1 summarizes a history of $\mu^- - e^-$ conversion in various nuclei.

Table 3.1: History and summary of $\mu^-{-}e^-$ conversion in various nuclei.

Process	90% C.L. upper limit	place	year	reference
$\mu^- + Cu \to e^- + Cu$	$< 1.6 \times 10^{-8}$	SREL	1972	[30]
$\mu^- {+}^{32}S \to e^- {+}^{32}S$	$< 7 \times 10^{-11}$	SIN	1982	[31]
$\mu^- + Ti \to e^- + Ti$	$< 1.6 \times 10^{-11}$	TRIUMF	1985	[32]
$\mu^- + Ti \to e^- + Ti$	$< 4.6 \times 10^{-12}$	TRIUMF	1988	[33]
$\mu^- + Pb \to e^- + Pb$	$< 4.9 \times 10^{-10}$	TRIUMF	1988	[33]
$\mu^- + Ti \to e^- + Ti$	$< 4.3 \times 10^{-12}$	PSI	1993	[34]
$\mu^- + Pb \to e^- + Pb$	$< 4.6 \times 10^{-11}$	PSI	1996	[27]
$\mu^- + Ti \to e^- + Ti$	$< 6.1 \times 10^{-13}$	PSI	1998	[5]

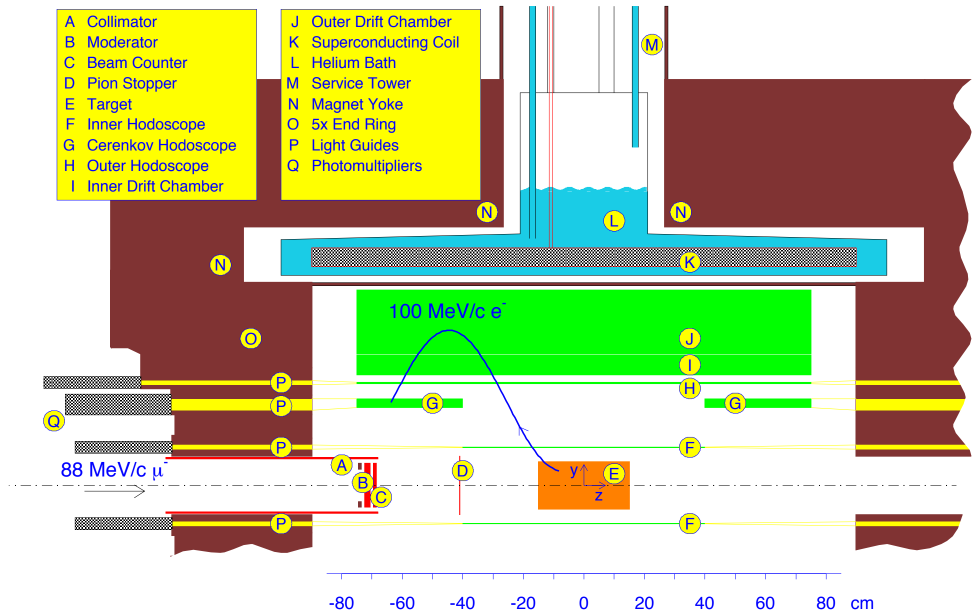

Figure 3.4: Schematic layout of the SINDRUM-II detector.

The SINDRUM II collaboration at PSI had carried out experiments to search for $\mu^{-}-e^{-}$ conversion in various nuclei. A schematic view of the SINDRUM II spectrometer is shown in Fig. 3.4. It consisted of a set of concentric cylindrical drift chambers inside a superconducting solenoid magnet of 1.2 T. Negative muons with a momentum of about 90 MeV/c were stopped in a target located at the center of the apparatus, after passing a CH_2 moderator and a beam counter made of plastic scintillator. Charged particles with transverse momentum (with respect to the magnetic field direction) above 80 MeV/c, originating from the target, first hit two layers of plastic scintillation arrays followed by two layers of drift chambers, before eventually hitting plexiglass Cherenkov hodoscopes placed at both ends. Charged particles having transverse momentum below about 80 MeV/c were contained inside, and could not reach the tracking region under a magnetic field of 1.2 T. A momentum resolution of about 2.8% (FWHM) for the energy region of conversion electrons was achieved. For the background rejection the following are used in an off-line analysis: the e^{-} energy (E_e), a time delay between the times of charged particle tracks in the spectrometer and the beam-counter signal (Δt), the position of the origin of the reconstructed trajectory (Δz) and the polar track angle. Events with small Δt were removed so as to reject prompt backgrounds, such as electron scattering and radiative pion capture.

In a 1993 run with a titanium target, a total of 3×10^{13} stopped μ^{-}s were accumulated at a rate of 1.2×10^{7} μ^{-}/s from the $\mu E1$ beam line at PSI. The overall

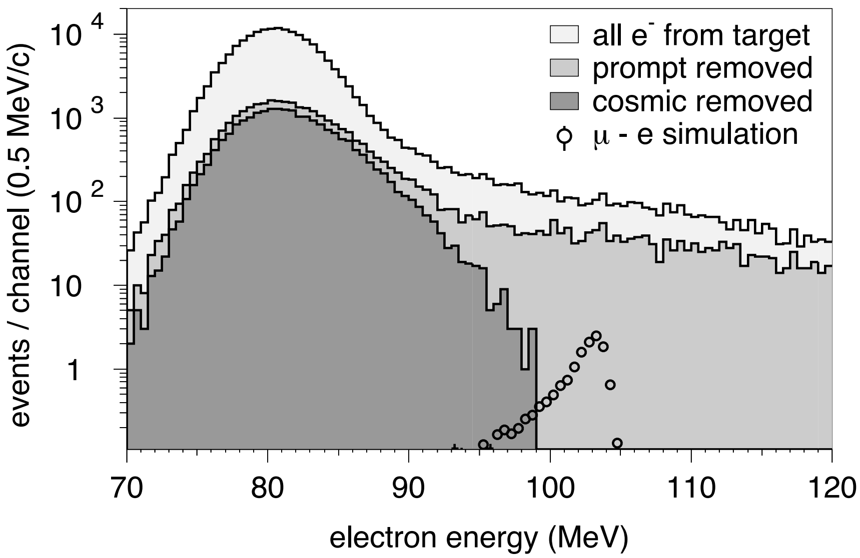

Figure 3.5: Electron momentum distribution for the $\mu^- + Ti \rightarrow e^- + Ti$ reaction, measured by the SINDRUM-II detector.

efficiency was about 13 %. The e^- momentum spectrum for the Ti target in the 1993 data is shown in Fig. 3.5, where the successive background rejections by prompt veto (*i.e.* Δt cut) and cosmic-ray suppression are shown. Since no events were found in the signal region, a 90% C.L. upper limit of 6.1×10^{-13} was obtained [5]. Also, for a lead target, it gave $B(\mu^- Pb \rightarrow e^- Pb) < 4.6 \times 10^{-11}$ [27]. Following this work, SINDRUM-II took data with a gold target and those with a lead target in 1997 and 1998, respectively. The data analysis is underway.

A new experiment (E940) at Brookhaven National Laboratory (BNL) AGS, called the MECO (Muon Electron COnversion) experiment, has been prepared [28]. MECO aims to search for $\mu^- + Al \rightarrow e^- + Al$ at a sensitivity below 10^{-16}. It will use a new high-intensity pulsed muon beam, which could yield about 10^{11} μ^-/s stopped in a target. A schematic layout of the MECO detector is shown in Fig. 3.6. The MECO apparatus consists of a superconducting (SC) solenoid magnet to capture pions from the production target (production solenoid), a curved transport SC solenoid magnet system (transport solenoid), and a SC solenoid spectrometer, which observes only the 105 MeV signal electrons (detector solenoid). Based on the solenoid capture scheme originally proposed by MELC [29], it has an axially graded magnetic field (from 3.5 T to 2.0 T) to efficiently capture pions from a tungsten target located on the axis of the solenoid magnet. The curved transport solenoid will capture muons from pion decays, and select the momentum and sign of charged particles by using collimators at three positions. Layers of thin aluminum targets where the μ^-s are stopped are placed in the detector solenoid with an axially graded magnetic field. The conversion electron

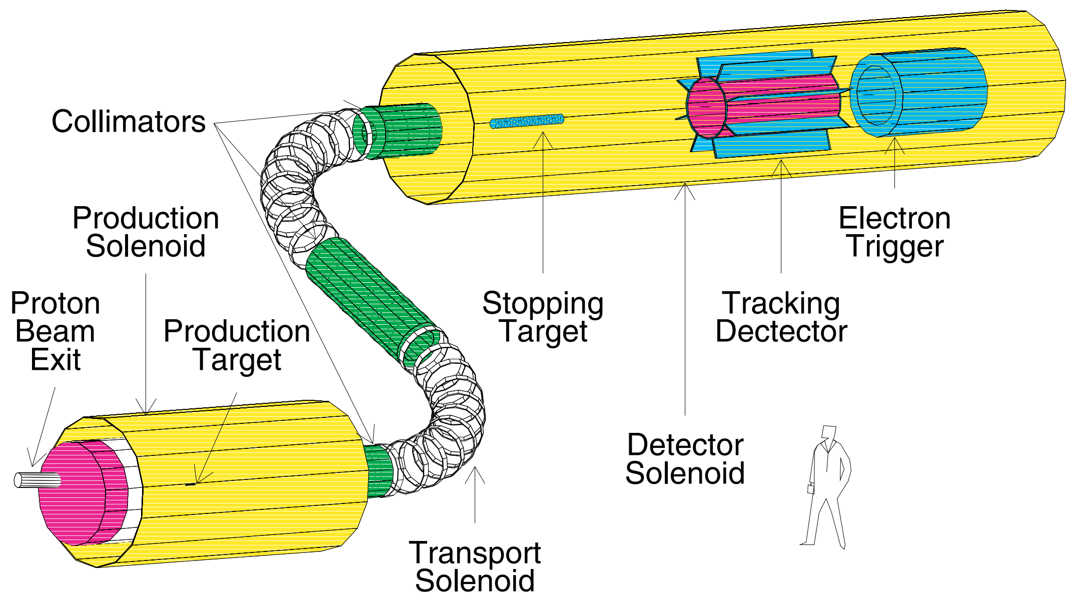

Figure 3.6: Schematic layout of the MECO detector.

of 105 MeV is momentum analyzed with a resolution of 900 keV(FWHM) and an acceptance of 25% in a straw tracking chamber. A pulsed proton beam of about 1 MHz repetition with a pulse length of 30 nsec can be extracted at the AGS. A high extinction between the beam pulses (the ratio of the number of protons between pulses to that in the beam pulse) of 10^{-9} is needed to eliminate severe beam backgrounds at a high rate. They expect to observe 5 signal events for $B(\mu^- Al \to e^- Al) \approx 10^{-16}$ during a one-year run, with an expected background of 0.4 events.

3.3.2 Experimental Status of $\mu^+ \to e^+\gamma$ Decay Search

A experimental search for $\mu^+ \to e^+\gamma$ was carried out by the MEGA collaboration at Los Alamos National Laboratory (LANL). The MEGA detector consisted of a magnetic spectrometer for the positron and three concentric pair-spectrometers for the photon. They were placed inside a superconducting solenoid magnet of a 1.5 T field. The positron spectrometer comprised eight cylindrical wire chambers and scintillators for timing. The positron energy resolution (FWHM) was from 0.5 MeV (0.95%) to 0.85 MeV (1.6%) for a 52.8-MeV e^+, depending on the number of helical loops of e^+ tracks. For the pair-spectrometer, each layer had lead converters, MWPCs, drift chambers and scintillators. The photon energy resolutions (FWHM) were 1.7 MeV (3.3%) and 3.0 MeV (5.7%) for the outer and inner Pb conversion layers, respectively. A surface μ^+ beam of 29.8 MeV/c was introduced along the detector axis, and was stopped in the muon-stopping target made of a thin tilted Mylar foil. All of the charged particles from muon decays were confined within the positron spectrometer. The intensity of the muon beam was 2.5×10^8/sec with a macroscopic duty factor

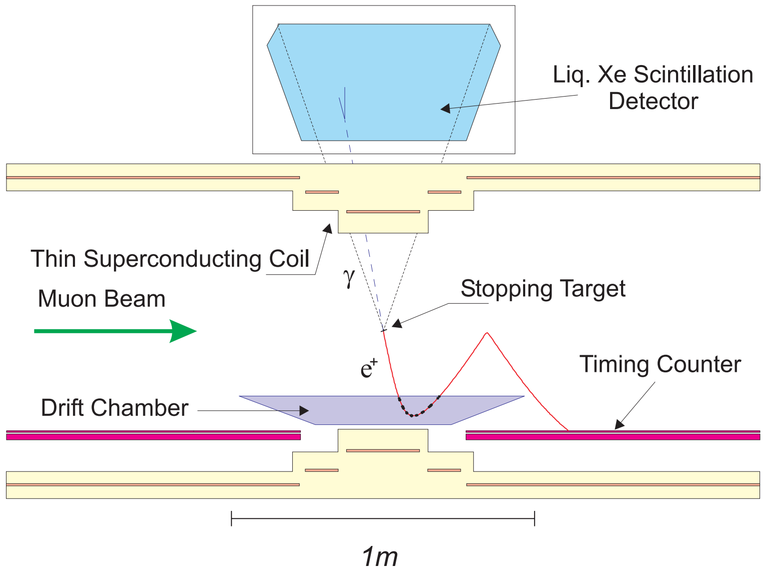

Figure 3.7: Schematic layout of the MEG detector.

of 6%. The total number of muons stopped was 1.2×10^{14}. By using the likelihood method, a new limit of 1.2×10^{-11} with 90% C.L. has been reported [3].

A new experiment called MEG at PSI, which aims at a sensitivity of 10^{-14} in the $\mu^+ \to e^+\gamma$ branching ratio, is under construction[35]. A schematic view of the detector is shown in Fig.fg:meg. The improvement will be expected by utilizing a continuous muon beam of 100% duty factor at PSI. With keeping the same instantaneous beam intensity as MEGA, the total number of muons available can be increased by a factor of 16. Further improvement is a novel liquid xenon scintillation detector of the "Mini-Kamiokande" type, which is a 0.8-m^3 volume of liquid xenon viewed by an array of a total of 800 photomultipliers from all the sides. The expected resolutions (FWHM) of the photon energy and position are about 1.4% and 4 mm, respectively. As the e^+ detection, a solenoidal magnetic spectrometer with a graded magnetic field is adopted, in which the magnetic field is arranged so that e^+ from the $\mu^+ \to e^+\gamma$ decay follows a trajectory with a constant radius, independently of its emission angle. It allows easier identification of the e^+ in the $\mu^+ \to e^+\gamma$ decay. Physics data taking is expected to start in year 2004 or later.

Chapter 4

Overview of The PRIME Experiment

The current limit for $\mu^-{-}e^-$ conversion is $B(\mu^- + Ti \rightarrow e^- + Ti) \leq 6.1 \times 10^{-13}$ from SINDRUM-II at PSI. Data with a gold target were also taken and analyzed at SINDRUM-II. Currently, the MECO experiment, which aims at a sensitivity of $B(\mu^- + Al \rightarrow e^- + Al) \leq 10^{-16}$, is being prepared at BNL-AGS.

However, to explore full discovery potential, another new generation experiment of $\mu^-{-}e^-$ conversion should be considered. Further improvements, we believe, could be achieved when a high-intensity muon source with narrow energy spread and small beam contamination (such as of pions and electrons) is realized.

The requirements to a muon beam to carry out a next-generation search for $\mu^-{-}e^-$ conversion process could be summarized as follows.

- **High Intensity**: The potential sensitivity achievable in searches for rare processes is ultimately limited by the number of muons available. Therefore, a high-intensity beam is essential. The muon beam intensity of $10^{11} - 10^{12}$ μ^-/sec should be required, yielding about more than $10^{20}\mu^-$ per year.

- **High Purity**: Beam contaminations are necessary to be removed, to reduce any background associated with them. It is already shown that the past experiments like SINDRUM-II have already seen a background event just above the signal region, and they suspect that it comes from pion contamination in a beam through radiative pion capture. Therefore, it is the most important to reduce pion contamination in a beam.

- **Narrow Energy Width**: Narrow energy spread of the beam will allow a thin muon stopping target to improve the momentum resolution of e^- detection, which is limited by energy loss in the muon stopping target.

- **High Resolution Spectrometer**: To improve the intrinsic momentum resolution in an e^- spectrometer, it is critical to construct a thin tracking chamber system.

We are aiming to improve the sensitivity further by additional factor of 100 from the MECO sensitivity, namely, in the order of 10^{-18} in the process of $\mu^- + Ti \rightarrow e^- + Ti$. Such an improvement is possible if we build a high intensity muon beam and a high resolution spectrometer.

Our experiment consists of the **PRISM beam**[1] and a **curved solenoid spectrometer**. Each of those will be explained in the following sections.

[1]A separate Letter of Intent on PRISM is available. Please refer to it for details.

Chapter 5

The PRISM Beam

A brief overview of the PRISM beam is presented. Its detailed description is presented in a separate Letter of Intent on PRISM.

5.1 PRISM Overview

PRISM is a project to provide a dedicated source of a high intensity muon beam with narrow energy-spread and small beam contamination. PRISM stands for "*Phase Rotated Intense Slow Muon source*". The aimed beam intensity is $10^{11} - 10^{12}\mu^{\pm}$/sec, four orders of magnitude higher than that available at present. It is achieved by large solid-angle pion capture with a high solenoid magnetic field. The narrow energy spread can be achieved by phase rotation, which accelerates slow muons and decelerates fast muons by an radio frequency (RF) field. The pion contamination in a muon beam can be removed by a long flight path of the beam in PRISM so that most of pions decay out.

PRISM consists of

- a pulsed proton beam (to produce a short pulsed pion beam),
- a pion capture system (with large-solid angle by a high solenoidal magnetic field),
- a pion decay and muon transportation system (in a long solenoid magnet of about 10 m long), and,
- a phase rotation system (which accelerates slow muons and decelerates fast muons by an RF field),

Some of the key components are explained in detail in the following sections. The conceptual structure of PRISM is shown in Fig. 5.1.

The PRISM beam characteristics are summarized in Table 5.1. A schematic layout of PRISM is shown in Fig. 5.2. One of the features of PRISM is to do phase rotation by a Fixed-Field Alternating Gradient synchrotron (FFAG), which has several advantages, such as a large momentum acceptance.

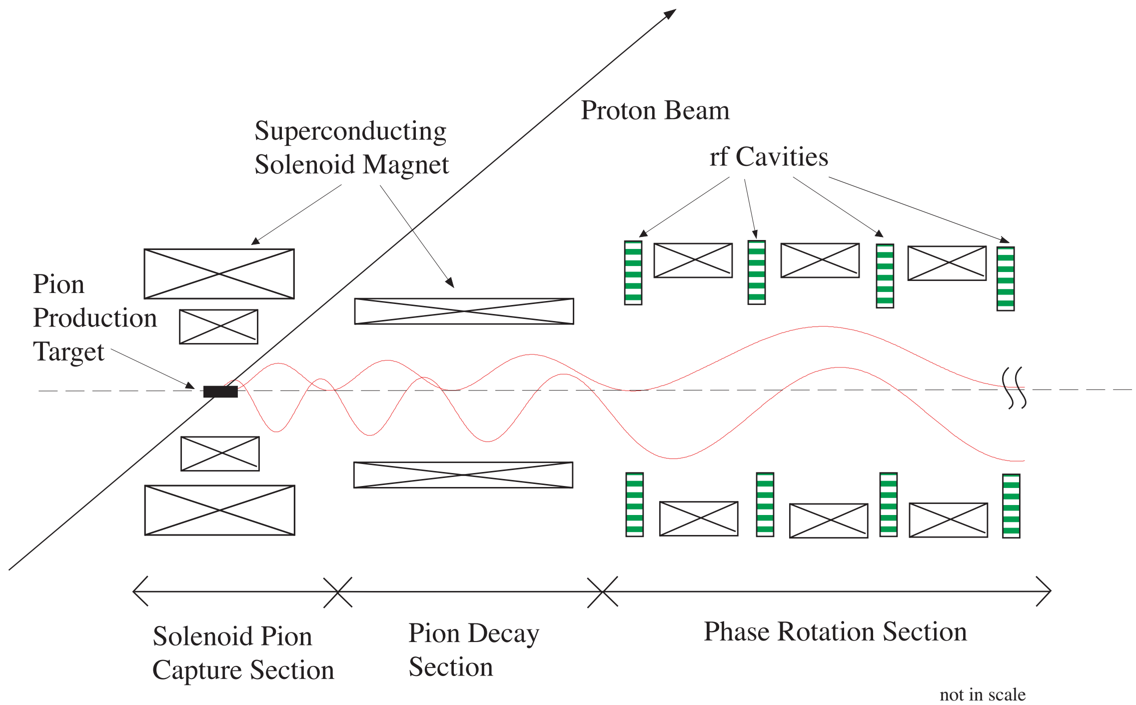

Figure 5.1: Conceptual Components of PRISM. It has the pion capture system, the pion decay and muon transport system, and the phase rotation system.

Table 5.1: Anticipated PRISM beam design characteristics

Parameters	Design goal	Comments
Beam Intensity	$10^{11} - 10^{12} \mu^{\pm}$/sec	10^{14} protons/sec is assumed.
Muon kinetic energy	20 MeV	$P_\mu = 68$ MeV/c
Kinetic energy spread	$\pm(0.5 - 1.0)$ MeV	
Beam Repetition	100 - 1000 Hz	

5.2 Estimated Muon Yields

The muon yield (Y_μ) at PRISM can be given by[1]

$$Y_\mu = N_p \cdot N_\pi \cdot \varepsilon_{\pi-decay} \cdot \varepsilon_{mom} \cdot \varepsilon_{time} \cdot \varepsilon_{emittance} \cdot \varepsilon_{dispersion} \cdot \varepsilon_{FFAG} \cdot \varepsilon_{\mu-decay}, \tag{5.1}$$

where N_p is a number of protons per seconds, N_π is a number of pions captured at the pion capture system per proton. ε_{mom}, ε_{time}, $\varepsilon_{emittance}$, $\varepsilon_{dispersion}$, ε_{FFAG}, $\varepsilon_{\pi-decay}$, and $\varepsilon_{\mu-decay}$ are, respectively, the momentum acceptance (50 MeV/c < P_μ < 90 MeV/c), the timing acceptance (of about ± 5 nsec), the beam emittance acceptance of the PRISM-FFAG ring, the efficiency of the dispersion matching between the muon

[1] The details can be found in the separate Letter of Intent on PRISM.

transport system and the PRISM-FFAG ring, the survival rate during 5 turns in the PRISM-FFAG, the pion decay rate, and the muon survival rate due to muon decay.

They can be estimated by using Monte Carlo simulations with the assumption of particular design based on some technologies employed. The technology choice has a large impact on the muon yield. In particular, N_{π} and $\varepsilon_{emittance}$ have strong dependence on the target material and length, the magnitudes of the pion capture field (capture field) and of the pion-decay and muon-transport system (transport field). Although we have not fully optimized, typical sampling cases are listed in Tables 5.2, where the numbers of muons per 10^{14} protons per second (J-PARC phase I) and 4×10^{14} protons per second (J-PARC phase II) are shown[2]. In this estimation, the 3-interaction target length of 120 cm and of 28.8 cm for graphite and tungsten respectively are used. The factor $\varepsilon_{\pi-decay}$ was included in Monte Carlo simulation of the pion capture system. The factor $\varepsilon_{\mu-decay}$ was estimated with another Monte Carlo simulation dedicated to the FFAG phase rotation, and it is about 60%. At the time of writing, detailed studies on $\varepsilon_{dispersion}$ and ε_{FFAG} have not been completed yet, and therefore they are assumed to be 100 %.

5.3 Pion Contamination in a Beam

At PRISM, a total flight length is about 150 meters. The survival rate $N^{\pi}_{\rm survival}$ is given by

$$N^{\pi}_{\rm survival} = \exp(-\frac{L}{c\beta\gamma\tau_{\mu}}) \tag{5.2}$$

where β, γ, and τ_{μ} are the Lorentz factors and the mean lifetime of the pion, respectively. For the pions of about 68 MeV/c, it gives

$$N^{\pi}_{\rm survival} \sim 10^{-17}. \tag{5.3}$$

Therefore, there is absolutely no pion contamination for the particles with 5 turns in the PRISM-FFAG ring. One of the issues is that when late pions, which come between the proton pulse, enter into the PRISM-FFAG ring, there would become pion contamination. To eliminate them, (1) the proton extinction between the pulses should be small (10^{-3}) and (2) the kicker magnet at the entrance of the PRISM-FFAG has to have additional extinction for late charged particles. Our naive estimation shows that the reduction of those late pions can be achievable at our desirable level of 10^{-18}.

[2] At 4 MW beam power (4×10^{14} protons per second), it is known that the solid targets, like graphite and tungsten, might not be able to be used. Several alternatives are discussed such as a mercury liquid jet, a rotating band target, a tantalum fine-particle target.

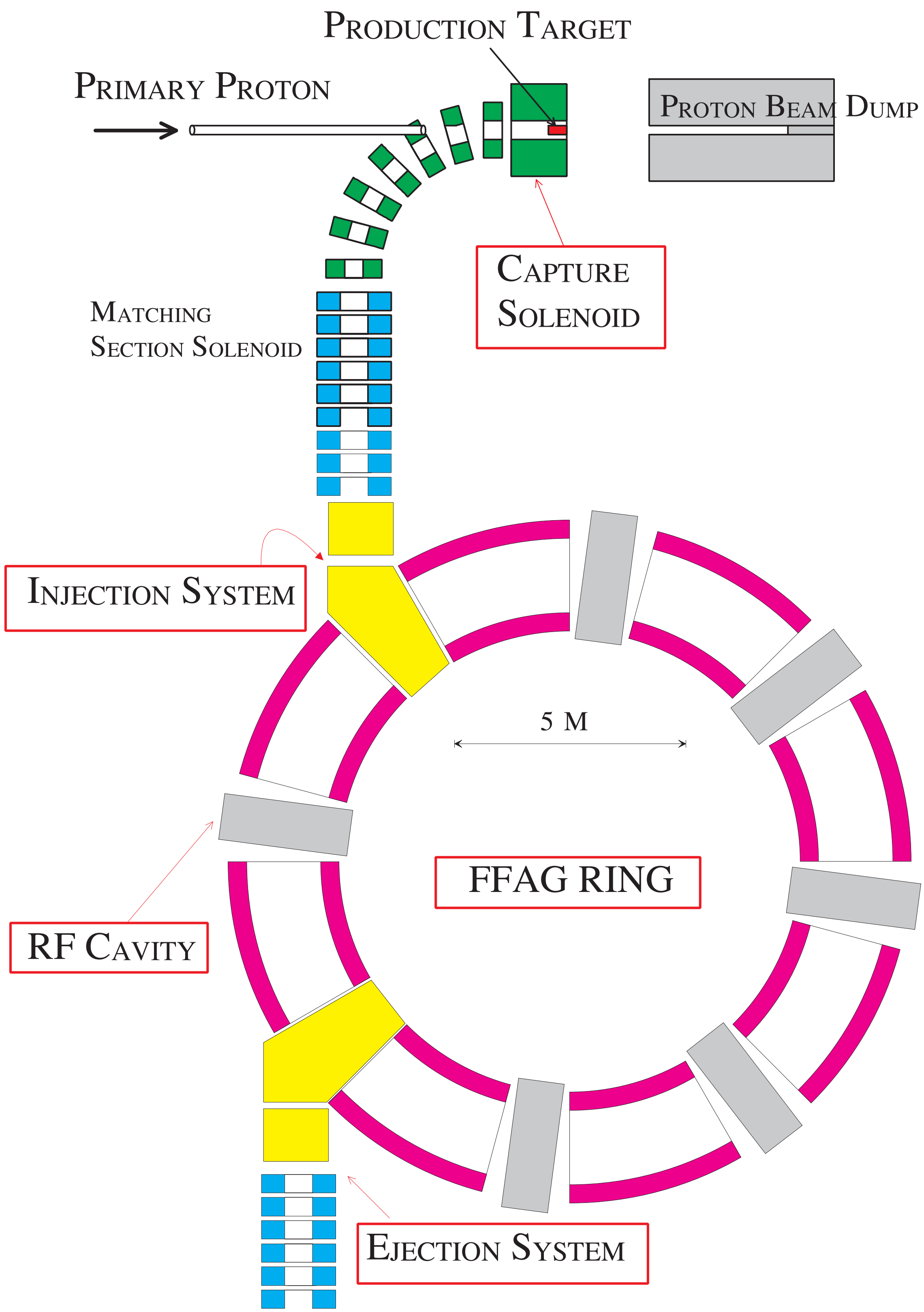

Figure 5.2: Schematic layout of PRISM.

Table 5.2: Negative Muon yields per second (Y_μ) for various target materials, pion capture magnetic fields, muon transport magnetic fields with 10^{14} protons/sec (J-PARC Phase-I) and 4×10^{14} protons/sec (J-PARC Phase-II). The top table is for $\varepsilon_{emittance}$ of 10,000 πmm·mrad in horizontal and 2,000 πmm·mrad in vertical, whereas the bottom table is for $\varepsilon_{emittance}$ of 20,000 πmm·mrad in horizontal and 3,000 πmm·mrad in vertical.

Target material	Capture field	Transport field	Muon yield per 10^{14} protons	Muon yield per 4×10^{14} protons
Graphite	16 T	4 T	2.4×10^{10}	9.6×10^{10}
	16 T	2 T	1.8×10^{10}	7.2×10^{10}
	12 T	4 T	1.8×10^{10}	7.2×10^{10}
	12 T	2 T	1.2×10^{10}	4.8×10^{10}
	8 T	4 T	1.8×10^{10}	7.2×10^{10}
	8 T	2 T	1.2×10^{10}	4.8×10^{10}
	6 T	4 T	0.6×10^{10}	2.4×10^{10}
	6 T	2 T	1.2×10^{10}	4.8×10^{10}
Tungsten	16 T	4 T	4.8×10^{10}	19×10^{10}
	16 T	2 T	5.4×10^{10}	22×10^{10}
	12 T	4 T	4.2×10^{10}	17×10^{10}
	12 T	2 T	4.2×10^{10}	17×10^{10}
	8 T	4 T	3.0×10^{10}	12×10^{10}
	8 T	2 T	3.0×10^{10}	12×10^{10}
	6 T	4 T	1.8×10^{10}	7.2×10^{10}
	6 T	2 T	2.4×10^{10}	9.6×10^{10}

Target material	Capture field	Transport field	Muon yield per 10^{14} protons	Muon yield per 4×10^{14} protons
Graphite	16 T	4 T	4.8×10^{10}	19×10^{10}
	16 T	2 T	3.6×10^{10}	14×10^{10}
	12 T	4 T	3.6×10^{10}	14×10^{10}
	12 T	2 T	3.0×10^{10}	12×10^{10}
	8 T	4 T	3.0×10^{10}	12×10^{10}
	8 T	2 T	2.4×10^{10}	9.6×10^{10}
	6 T	4 T	1.8×10^{10}	7.2×10^{10}
	6 T	2 T	1.8×10^{10}	7.2×10^{10}
Tungsten	16 T	4 T	13×10^{10}	50×10^{10}
	16 T	2 T	11×10^{10}	46×10^{10}
	12 T	4 T	9.6×10^{10}	38×10^{10}
	12 T	2 T	9.0×10^{10}	36×10^{10}
	8 T	4 T	6.0×10^{10}	24×10^{10}
	8 T	2 T	7.2×10^{10}	29×10^{10}
	6 T	4 T	4.2×10^{10}	17×10^{10}
	6 T	2 T	4.8×10^{10}	19×10^{10}

Chapter 6

The Proposed Detector

6.1 Overview

In this section, we describe a candidate detector for the PRIME experiment in detail. The sole role of the detector is to select the genuine $\mu^- - e^-$ conversion signal from a huge number of background events. The signature of the $\mu^- - e^-$ conversion signal is clear, namely, a mono-energetic ($\sim$105 eV) electron coming from the muon stopping target. By contrast, background events have various origins, and are huge.

It is useful to categorize background events. One type is a so-called "intrinsic background", which stems from $\mu^- - e^-$ decays in orbit. For a Ti target, about 15% of the muons bounded in an atomic orbit end up with this process. The energy spectrum of the ejected electrons resembles the Michel spectrum. But, due to nuclear recoil, its high energy tail extends up to the energy of the signal. The only way to distinguish the signal from this type of background is to measure the electron energy as precise as possible. The signal, if it exists, would stand up as a peak over the decay-in-orbit background spectrum. We expect it necessary to achieve an energy resolution of 350 keV(FWHM) when the branching sensitivity of 10^{-18} is to be reached.

Other types of background events come from various sources: $\pi^-/\bar{p}$ capture or scattering of electrons in the targets, and cosmic rays, etc. Generally speaking, the energy spectrum of these backgrounds is broad and spreads over the signal energy region. Rejection of these backgrounds must be individually considered. In our experiment, the backgrounds due to $\pi^-/\bar{p}$ captures can to be reduced to a negligible level by reducing their contaminations in the beam. The background events due to cosmic rays can be decreased by active and/or passive shields. In addition, the duty factor of the PRISM beam makes the cosmic ray events smaller. The electron scattering events can be safely neglected if the electron energy in the beam is less than the signal energy. Since the highest electron energy comes from a muon decay in the forward direction, the muon momentum should be less than 77 MeV/c. On the other hand, the muon beam momentum from PRISM is expected to be 68$\pm$2 MeV/c, which is well below the 77 MeV/c and thus the electron scattering background might be negligibly small. The background rejection will be explained in detail in Chapter 7.

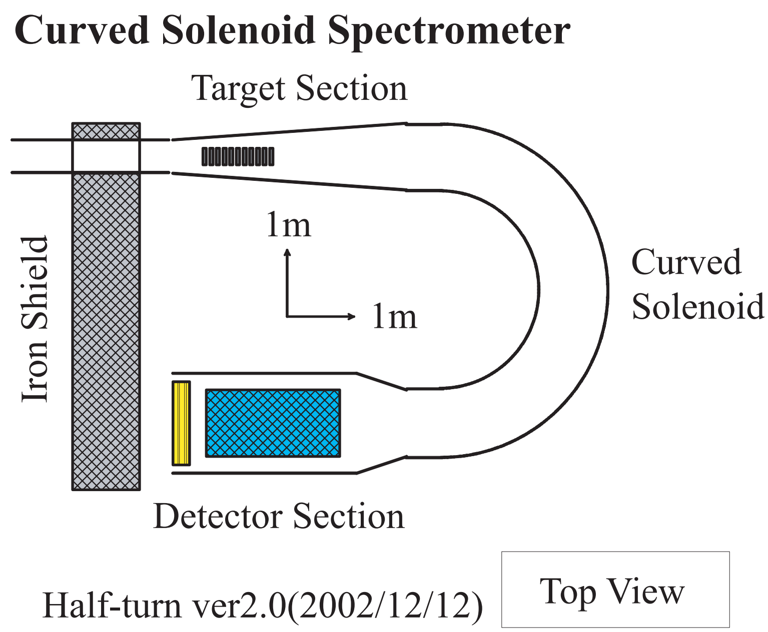

Figure 6.1: Setup of a proposed spectrometer.

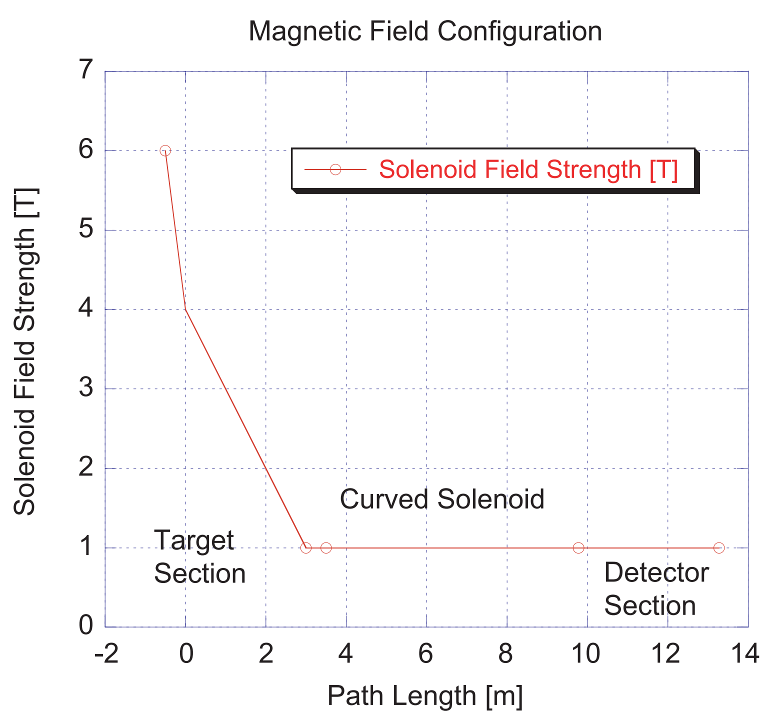

Figure 6.2: Magnetic Configuration of the spectrometer.

One of the potential drawback of using the PRISM beam is its low duty factor. The repetition of the PRISM beam is ∼10 pulse/cycle in the entry stage, and ∼100 pulse/cycle at its upgrade. Thus, the instantaneous beam intensity is about $10^{10} \sim 10^{11} \mu^-$ per bunch. The measurement time window opens for about a μsec. Any detector using the PRISM beam must be able to handle this instantaneous intensity. To summarize, the requirements for the detector are

1. capability of handling a very high instantaneous rate,
2. good energy resolution to distinguish the $\mu - e$ conversion signal from electrons coming from decay-in-orbit, and
3. good rejection of background events.

In the PRIME experiment, we consider to employ a curved solenoid spectrometer, which would meet the requirements listed above. As shown in Fig. 6.1, the curved solenoid spectrometer consists of three sections; a target section, a curved solenoid section, and an electron detection section. Each section will be described in detail below.

6.2 Magnetic Field

In this section, the magnetic field configuration is described briefly. In the target section, a graded solenoid field is employed, as in the MECO experiment. The magnitude of the graded field starts with 6 T at about 0.5 m upstream of the target, and becomes 4 T at the muon stopping target location, and goes down to 1 T at the entrance of the curved solenoid. In the curved solenoid, toroidal magnetic field is produced. Its major and minor radius are 2 m and 0.5 m respectively. The strength of the magnetic field is 1 T along the central orbit. As will be explained shortly, a vertical (normal to the bending plane) magnetic filed of 0.18 T is superimposed to the toroidal field. An uniform solenoidal field is arranged at the detector section. The strength of the magnetic field as a function of track path is shown in Fig.6.2.

It will be useful to mention the property of a particle motion in a graded solenoid field. If solenoid magnetic fields change adiabatically, a quantity of $p_\perp^2/B$ is conserved [37], where $p_\perp$ is a particle's momentum transverse to a solenoid field B. Namely

$$\frac{\sin^2\theta_{in}}{B_{in}} = \frac{\sin^2\theta_{out}}{B_{out}}$$

is constant, where θ is a track angle with respect to its central trajectory. The suffixes *in* and *out* imply two different positions. Fig. 6.3 shows the relation of two polar angles. In this figure, the dashed curve corresponds to the case of B_{in}=4 T and B_{out}=6 T, while the solid curve (below) to the case of B_{in}=4 T and B_{out}=1T. If B_{out} is larger than B_{in}, the magnetic field acts as a mirror. For example, any particles produced with 55° or more in the backward direction are reflected back to the target point. This mirror effect is useful to increase acceptance of the spectrometer. Although the signal electrons are emitted isotropically from the target, once a mirror field is employed, about 80% of the $\mu - e$ conversion electrons enter the spectrometer located downstream.

Since the magnetic field is reduced to 1 T at the entrance of the curved solenoid, the maximum polar angle is less than 30°, as is shown in Fig. 6.3. This is important for the curved solenoid spectrometer to work as an efficient momentum selector.

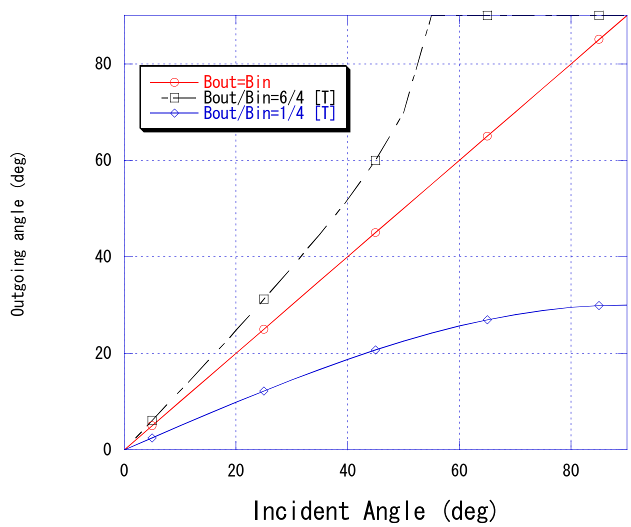

Figure 6.3: Relation between the incident ant outgoing angles in a graded solenoidal field.

6.3 Muon Stopping Target

The muon stopping target must be designed to maximize the stopping probability of the muons and the acceptance of the $\mu^- - e^-$ conversion electron to the spectrometer. Also, it should be designed to minimize the energy loss of the $\mu^- - e^-$ conversion electron as they exit the target in order to improve the momentum resolution of the electrons. It would be also important to have the smallest possible target size to reduce any kinds of possible backgrounds.

Thus, the stopping target configuration is critical. Major parameters to be considered are material, thickness, size (diameter), a number of layers, a distance between adjacent layers (spacing), and a magnetic field and its gradient. We have considered various target configurations. Our tentative target configuration is to use 20 layers of 50 μm thick Ti foils. The diameter of those targets is 50 mm, and they are spaced by 5 cm one another.

6.3.1 Range of muons

One of the significant features of using the PRISM muon beam is to have narrow momentum spread. According to the present PRISM design, a momentum spread of $\pm$ 3 % with the central momentum of 68 MeV/c (being equivalent to 20 MeV in kinetic energy) is expected after phase rotation.

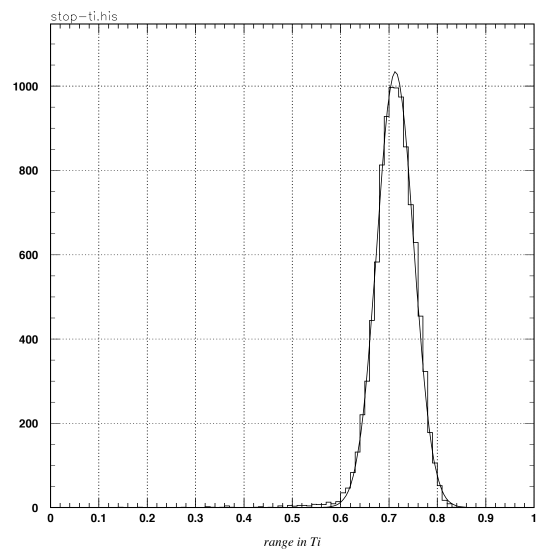

Figure 6.4: Range of muons of 68 MeV/c with $\pm$ 3 % momentum width. The range distribution is about 380 μm in sigma.

To examine a muon-stopping target needed to stop such a muon beam, Monte Carlo simulations based on GEANT3 have been done. In this particular simulations, a range of muons in Ti was examined by taking account of range straggling and multiple scattering. A preliminary result is shown in Fig. 6.4, where a range width is about 380 μm in sigma. The input beam is a parallel beam whose momentum distribution is uniform in the momentum range of $\pm$ 3 % with 68 MeV/c central momentum. It implies that a Ti target of 1 mm in total thickness is sufficient to stop about 80 % of the beam muons.

The present range width is not dominated by range straggling nor multiple scattering, but dominated by the momentum distribution in the beam muons. Fig. 6.5 shows range distribution as a function of muon momentum, where it is clearly seen that the muon-momentum distribution determines the total range width, and the effects from range straggling is smaller. If the performance of phase rotation at PRISM gets better, there is still a room to get a muon-stopping target thinner by a factor of two at most (to about 500 μm full width).

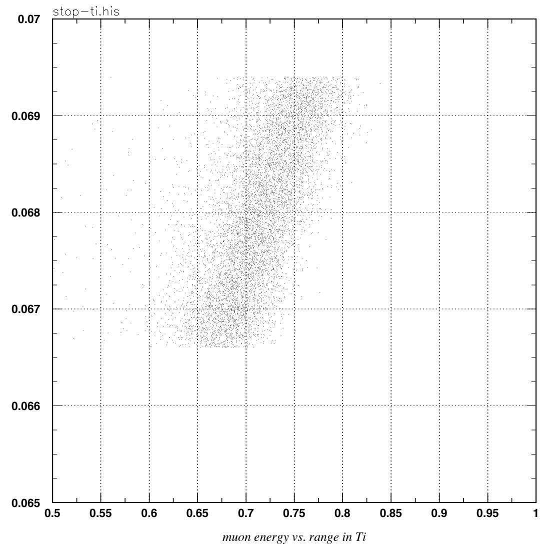

Figure 6.5: 2-dimensional plot of muon momentum (vertical) vs. range (horizontal). The effects from range straggling is smaller than the momentum spread.

One choice is to have multi-layers of thin disks. One case is to use 20 layers of 50 μm Ti disks with about 80 % stopping efficiency. Note that 17−25 layers of 200 μm aluminum thin disks with 5 cm separation are going to be used in the MECO experiment with about 56 % stopping efficiency.

6.3.2 Energy Loss of Outgoing Electrons

Fig. 6.6 shows a distribution of the traversed thickness for the case of the 105 MeV/c signal electrons. The events toward the upstream histogrammed on the bin at -0.001 for convenience. (The fraction of those events is about 20%, as explained above.) Fig. 6.7 shows GEANT-simulated energy loss in a 50μm Ti target for the electrons impinging normally. Several relevant numbers can be extracted from the plot; the most probable energy loss is $(\Delta E)_{mp} = 12$ keV, the median is 14 keV, and an average energy loss, excluding the largest 1% of events which are due most likely to Bremsstrahlung, is $(\Delta E)_{av}^{99\%} = 17$ keV. From these two plots, we can infer an average energy loss in the target section. For example, if we want to restrict particle's energy loss to be less than 150 keV, then the total thickness traversed should be 450 μm or less. Here we used $(\Delta E)_{av}^{99\%}$ in calculating the average energy loss. From Fig. 6.6, about 54.8% of particles generated in the targets go forward with $(\Delta E)_{av}^{99\%} < 150$ keV. There is no strong dependence upon the target position for those electrons.

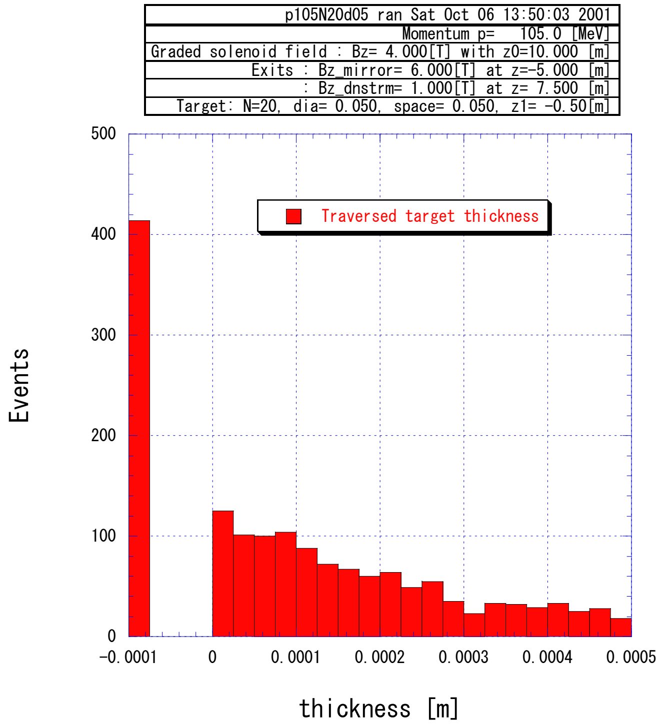

Figure 6.6: Target thickness traversed by signal electrons.

6.4 Curved Solenoid Spectrometer

6.4.1 A Principle of Curved Solenoid Spectrometer

The curved solenoid spectrometer is a magnetic system to select a charged particle with a desired momentum. Its main features are a large acceptance and a good rejection power. In the section, we present the curved solenoid spectrometer itself, and some study results of its performance. First of all, its principle is explained. It is well known that charged particles move in a helical motion around magnetic fluxes in a solenoidal field. When the solenoid is curved, as in a toroidal field, they drift normal to the bending plane. A drift distance D is given by

$$D = \frac{1}{qB_0}\left(\frac{s}{r_0}\right)\left(\frac{p_\parallel^2 + \frac{1}{2}p_\perp^2}{p_\parallel}\right),$$

where B_0 represents a magnetic field, r_0 is a radius of the toroid, s is a path length along the particle's central orbit, and $p_\parallel(p_\perp)$ represents respectively particle's parallel (perpendicular) momenta. This drift can be compensated by an auxiliary field imposed along the drift direction. Its value is represented by

$$B_{aux} = \frac{B_0 v_\parallel}{\omega_B r_0}\left[1 + \frac{1}{2}\left(\frac{p_\perp}{p_\parallel}\right)^2\right]$$

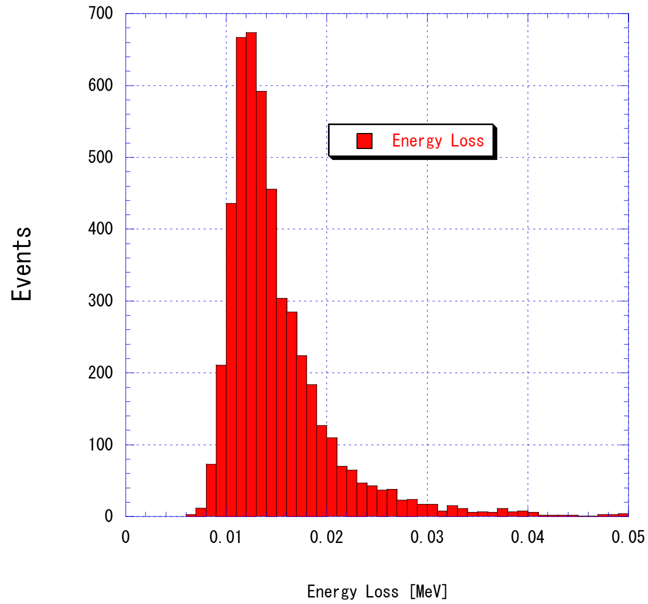

Figure 6.7: Energy loss distribution in a 50 μm-thick target.

with $\omega_B = qc^2 B_0/E_e$. For example, if r_0 is set to 2 m, B_{aux}=0.18 T for the signal electron with $\tan\theta = p_\perp/p_\parallel = 0$. In order to use this toroidal field as a spectrometer (or a momentum filter), it is essential to remove particle's polar angle dependence (θ). In our case, since the polar angle θ_z is less than 0.5 at the entrance, the contribution of the $\tan\theta$ term is small. Thus, this toroid field act as an efficient momentum selector, as will be shown in the next subsection.

6.4.2 Transport Efficiency

Fig.6.8 shows an example of tracks in the curved solenoid spectrometer. The track with desired momentum (105 MeV/c) stays in the same horizontal plane, thanks to the auxiliary field, although it undergoes circular motion in the solenoidal field. On the other hand, a track with a wrong momentum (85 MeV/c for example) drifts downwards. Since the vertical drift distance D depends upon particle's momentum, unwanted particles can be eliminated by placing appropriate blocker(s) in the solenoid. Fig. 6.9 shows a distribution (Z-min), the minimum drift in the Z-direction recorded in the curved section. Considering the background rate, we have decided to place a blocker that removes the particles with $Z_{min} < -0.15$ m. Fig. 6.10 shows fraction of the particles that reach the detector section as a function of their momentum. It is found that about 53 % can be tranported successfylly while keeping the background

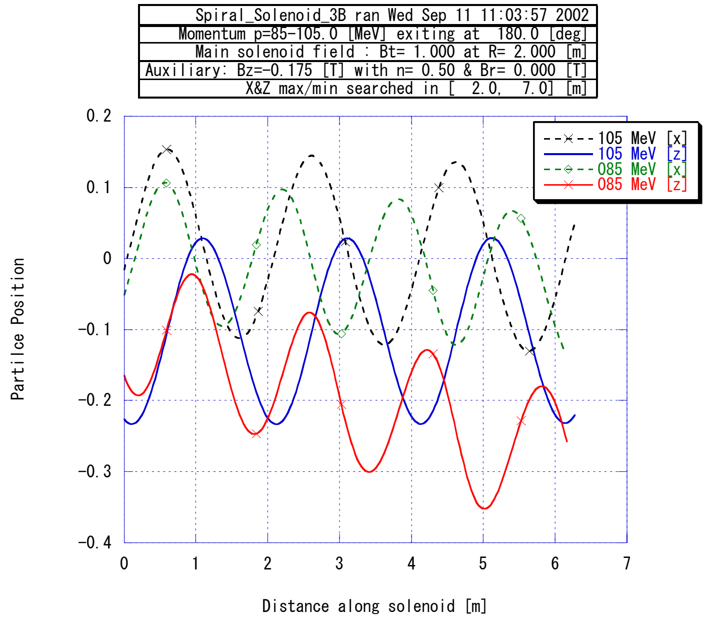

Figure 6.8: Example of tracks in the solenoid.

rate sufficiently low. Thus it is concluded that the curved solenoid spectrometer is quite efficient to remove unwanted particles.

6.5 Electron Detector

6.5.1 Overview

The main purpose of the electron detector is to identify electrons and to measure their energies. One example of the detector system is shown, although it is possible to be replaced by better one later.

The electron detector consists of a tracker, trigger scintillators, and an electromagnetic calorimeter. Two issues are important when considering the electron detector. The first is a number of particles par pulse entering the detector. If this number is large, the detector would not be able to distinguish the signal from backgrounds. The second is the detector energy resolution. The goal of the energy resolution is 350 keV (FWHM). Brief description for each detector component is shown in the following.

6.5.2 The Tracking Detector

The tracking detector consists of multiple sets of (planer) tracking chambers (TC0-TC9). They are installed in the detector solenoid, covering the entire solenoid aperture. One candidate is a straw-tube tracking chamber of thin wall thickness, such

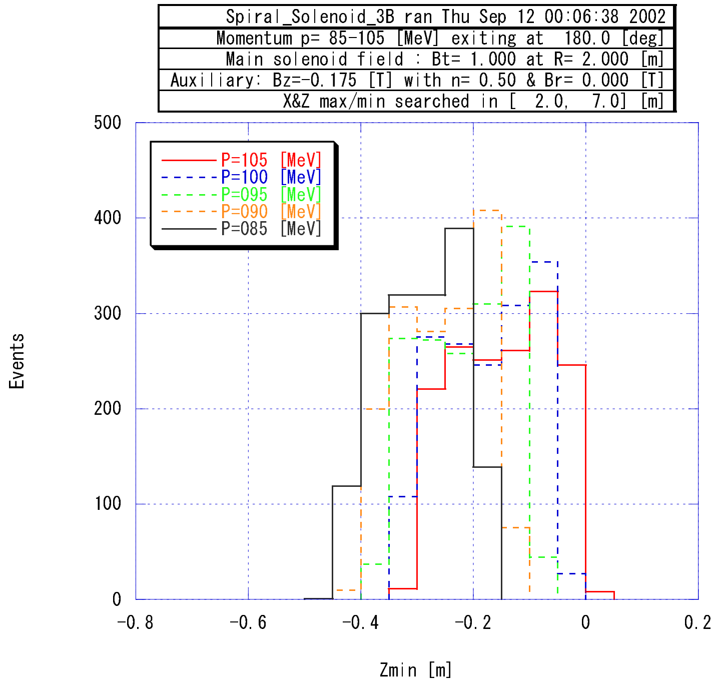

Figure 6.9: Zmin distribution in the solenoid.

as 25 μm. Since the momentum resolution of the tracking detector is dominated by multiple Coulomb scattering, a low mass chamber is demanded. Since the tracking detector has to be placed in vacuum, an ordinary planer chamber with a large area is difficult to install. Therefore, a straw tracking chamber is the best.

One set might consist of three layers (u, v and w) of straw tracking chambers. Each straw chamber has a 5-mm radius. To increase redundancy, a pair of sheets of cathode strips could be possibly placed upstream and downstream sides from the tracking layers. Induced charges on the cathode strips are used to determine the coordinate along the straw axis. As discussed in Appendix A, we have already carried out an R&D of straw tracking chambers, in particular, seamless straw-tube tracking chamber, The details can be presented in the appendix. From our R&D work, an anode position resolution of 100 μm and a cathode position resolution of 250 μm were obtained.

6.5.3 The Trigger/Energy Detector

The main purpose of this trigger/energy detector is to determine precisely a timing of the track, at the same time, determine a total energy of the track. One candidate is a plastic scintillator followed by either a lead-scintillator sandwich detector or an inorganic crystal detector. There will be about 5 tracks in the detector within the measurement time of 1 μsec per single burst of the muon beam pulse. Therefore, seg-

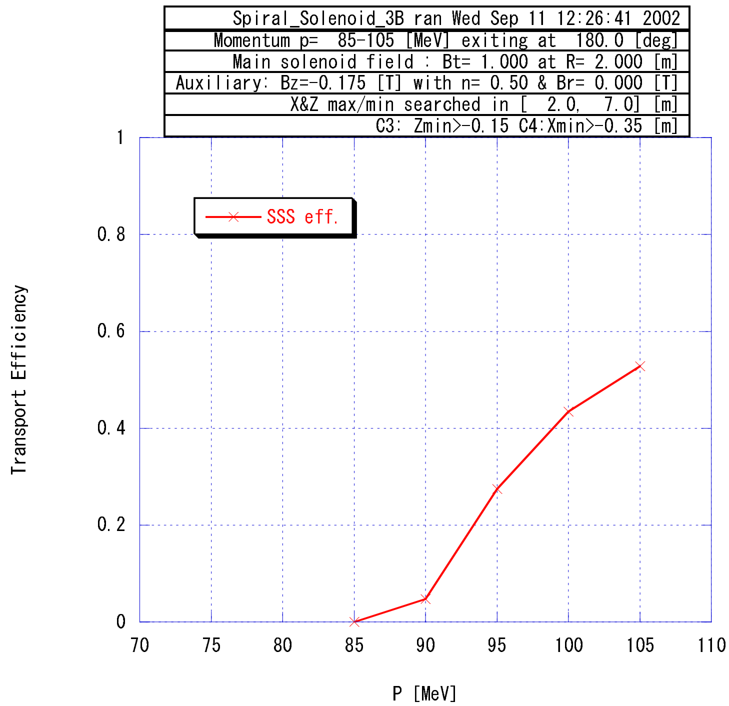

Figure 6.10: Curved solenoid transport efficiency. The cut values on Zmin and Xmin are $Zmin > -0.15$ and $Xmin > -0.35$, respectively.

mentation would be desired to reduce overlapping. The segmentation would also give additional hit position which would help reconstruction of the tracks. By comparing the energy (which is measured at the trigger/energy detector) and the momentum (which is measured at the tracking detector) of the tracks, the particle identification can be made.

6.5.4 Trigger and Data Acquisition System

A trigger signal to a data acquisition system is formed by the coincidence signal between the trigger counter and the electromagnetic calorimeter. Since we expect about 10 particles maximum to enter the detector, no "fast" electron is possible. All of them must be read in the DAQ computer using a pipe-line data acquisitions system.

6.5.5 Detector Rates

Complete tracks entering the detector are expected to be dominated by decay-in-orbit electrons. Positively charged particles and neutrals would be filtered out, to a large extent, by the curved solenoid spectrometer. In order to estimate a number of the particles entering the detector section, the decay-in-orbit electron spectrum shown in the MECO proposal was used.

Convoluting this spectrum with the efficiency in Fig. 6.10, and assuming that 10^{10} muons per pulse stop and decay in the target, we have obtained a number of the particles going into the detector to be about 5, no more than 10. Considering segmentation of the tracking chambers, and the fact that these events come in a time interval of ~ 1 μsec, it is concluded that the detector could handle this rate.

6.5.6 Momentum Resolution

Monte Carlo simulations have been made to examine the momentum resolution of electrons in the spectrometer. The position resolutions of the tracking chamber are assumed to be 100 μm in xy directions. The $\mu^- - e^-$ conversion electrons of 104.3 MeV were generated uniformly at the muon-stopping target. The energy loss in the target makes a long tail in low energy. Fig. 6.11 shows the fitted momentum distribution at the spectrometer.

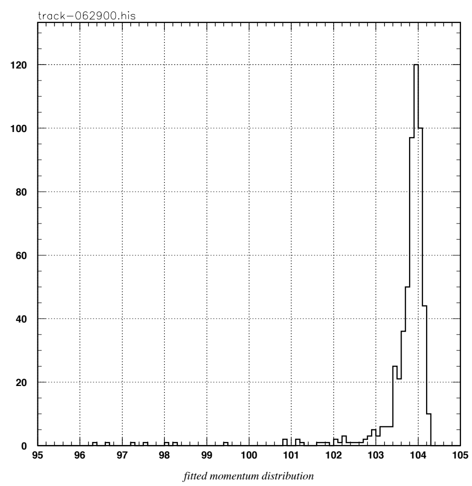

Figure 6.11: Fitted momentum distribution at the spectrometer.

To examine the intrinsic momentum resolution, difference of the fitted momentum from the true momentum at the spectrometer is shown in Fig. 6.12(a). From Fig. 6.12(a), the intrinsic momentum resolution of about 100 keV (FWHM) has been obtained. Fig. 6.12(b) shows the difference of the fitted momentum from the true momentum at birth (namely 104.3 MeV). The net momentum resolution is about 235 keV (FWHM). The net momentum resolution is dominated by the energy loss in the target.

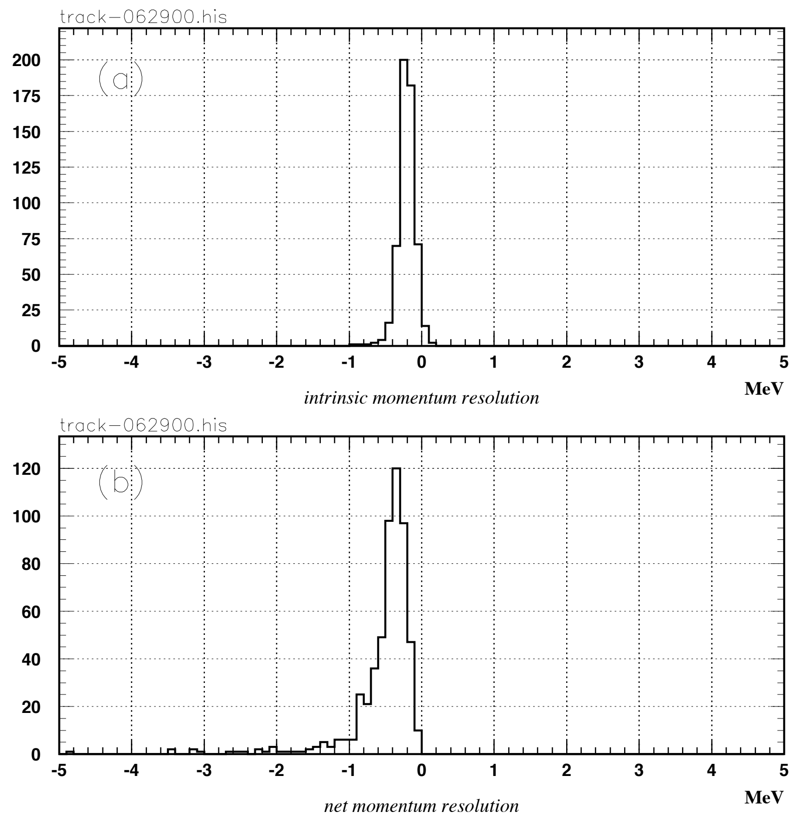

Figure 6.12: (a) Intrinsic momentum resolution at the spectrometer (100 keV FWHM) and (b) net momentum resolution with energy loss in the target (235 keV FWHM).

6.6 Detection Acceptance

The detector acceptance is estimated. The followings are considered : (1) geometrical acceptance at the target, (2) a transport efficiency of the spectrometer, and (3) requirement of particle's polar angle in the electron detector section. The other factors, which might affect the signal sensitivity, such as a stopping target efficiency, and a cut efficiency related to energy loss in the target, are not included here. Table 6.1 summarizes the results of our study. Elections will be emitted from the stopping target uniformly. Some of the electrons emitted in the backward would not come into the curved solenoid spectrometer. Due to the magnetic mirror effect, the geometrical acceptance to enter the spectrometer amounts to 80%, as was already described. The transport efficiency of the spectrometer of 53% was already described. The last item is the requirement for the electrons to have a large polar angle θ at the detector region. If the polar angle is small, the electron momentum would not be analyzed with sufficient resolution since a radius of the helix becomes too small to be measured.

We placed a condition to the electron's polar angle θ being $\sin\theta > 0.33$, which corresponds to $p_t > 86$ MeV/c for the signal electron at the target region. This requirement results in the acceptance of 80%. Multiplying these factors, we have obtained 35% for a net of geometrical acceptance.

Table 6.1: Geometrical acceptance of the proposed spectrometer.

Condition	Section	Fraction	Net acceptance	Remark
Forward direction.	target	79.3%	79.3%	
Blocker cut (vertical)	curved solenoid	53.0%	42.0%	Zmin>-0.15
Blocker cut (horizontal)	curved solenoid	100%	42.0%	Xmin>-0.35
$\sin\theta > 0.33$	detector	82.3%	34.6%	

Chapter 7

Background Estimation

7.1 Background Overview

Potential background sources to a search for $\mu^- - e^-$ conversion will be discussed here. They are listed and categorized as follows.

1. Intrinsic Physics Backgrounds
   - Muon decay in orbit of a muonic atom,
   - Radiative muon capture,
2. Beam-related Prompt Backgrounds
   - Radiative pion capture,
   - Scattering of electrons in a beam
   - Pion decay in flight
   - Muon decay in flight
   - Antiproton interaction
3. Non-Beam-related Backgrounds
   - Cosmic-rays
4. Others
   - Wrong electron track pattern recognition due to accidental hits

The background rates have been estimated for the case of a titanium (Ti) muon-stopping target[1]. It would be compared with the aluminum target in the MECO (BNL-E940) experiment. The estimations are presented in the following sections.

[1] In this Letter of Intent, a Ti target is arbitrarily selected. Further examination of the target selection will be made to optimize the sensitivity and backgrounds.

7.2 Muon Decay in Orbit

Muon decay in orbit is one of the important background sources in the search for $\mu^-{-}e^-$ conversion in a muonic atom, since the end point of the electron spectrum comes close to the signal region of $\mu^-{-}e^-$ conversion. Only the high-energy end of the electron energy spectrum is of interest for $\mu^-{-}e^-$ conversion experiments. At the high-energy end, the effect of the nuclear-recoil energy plays an important role (on its phase space). There have been several studies on its electron energy spectrum with nuclear-recoil energy taken into account. With the approximation of a constant nuclear-recoil energy, the electron spectrum with an expansion in powers of the electron energy (E_e) at the end-point energy is given by

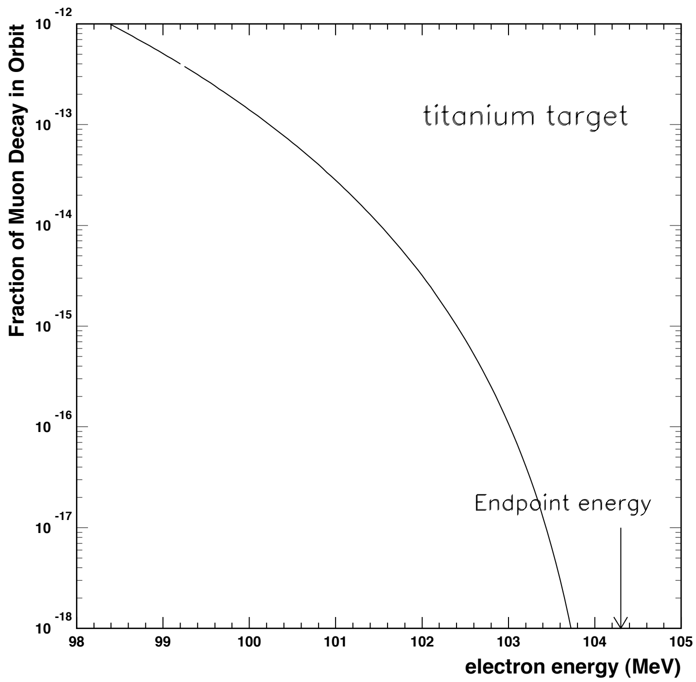

Figure 7.1: Energy spectrum of muon decay in orbit for Ti. The electron energy in $\mu^-{-}e^-$ conversion in Ti is also shown.

$$N(E_e)dE_e = \Big(\frac{E_e}{m_\mu}\Big)^2\Big(\frac{\delta_1}{m_\mu}\Big)^5\Big[D + E\cdot(\frac{\delta_1}{m_\mu}) + F\cdot(\frac{\delta}{m_\mu})\Big]dE_e, \tag{7.1}$$

where $\delta = E_{\mu e} - E_e$ and $\delta_1 = (m_\mu - B_\mu) - E_{rec} - E_e$. $E_{\mu e}$ is the e^- energy of the $\mu^-{-}e^-$ conversion signal defined in Eq.(3.4). E_{rec} is the nuclear-recoil energy given by $E_{rec} \approx E_e^2/(2M_A)$. It should be stressed that the spectrum falls off sharply as the fifth power of δ_1 toward its end point. The coefficients D, E and F as well as the end-point energy are tabulated in [38]. The contributions of the E and F terms to the total rate are about 4% and 8% respectively for $Z = 29$ and $E_e = 100$ MeV. Eq.(7.1) agrees with those in [39] and [40]. In the evaluation of the leading term D, important are (1) the use of a correct electron wave function incorporating the finite nuclear charge distribution, (2) the use of the Dirac muon wave function, and (3) the use of the small component of the muon relativistic wave function. In particular, the effect of (1) is large.

We have estimated the background rate from a muon decay in orbit. In the MECO experiment, the signal region is set to be above $E_e = 103.9$ MeV with the energy resolution of 900 keV. They have about 0.05 background events at a sensitivity of 10^{-16}. In the PRIME experiment, assuming we could reduce the width of the signal region by factor 2.5 due to the better net energy resolution of 350 keV(FWHM) than that in MECO (900 keV FWHM), we have about 0.05 background events at a sensitivity of 10^{-18}. It will be significantly reduced, if a better energy resolution than 350 keV is obtained.

7.3 Radiative Muon Capture

Radiative muon capture, $\mu^- + (A, Z) \rightarrow \nu_\mu + (A, Z-1) + \gamma$, followed by asymmetric e^+e^- conversion of the photon is another background. The kinematical endpoint (E^{kin}_{rmc}) of radiative muon capture (RMC) is given by

$$E^{kin}_{rmc} \approx m_\mu - B_\mu - \Delta_{Z-1}, \tag{7.2}$$

where Δ_{Z-1} is the difference in the nuclear binding energy of the initial (A, Z) and final $(A, Z-1)$ nucleus involved in radiative muon capture. Therefore, an appropriate target with a large Δ_{Z-1} can be selected so as to keep a wide background-free region for the coherent signal. Practically, the empirical endpoint of RMC (E^{emp}_{rmc}), which is evaluated by taking account of the RMC spectrum shape given by Primakoff's formula [41], is used. The E^{emp}_{rmc} values for Ti were estimated from the observed RMC on ^{40}Ca [42]. They are 89.7 MeV and 91.4 MeV for ^{48}Ti and ^{46}Ti respectively [43], whereas $E_{\mu e}$ is 104.3 MeV.

In the MECO experiment, the target material is aluminum and the thickness of each target disk is about 200 μm. The E^{emp}_{rmc} values for Al is 102.5 MeV, and the probability of producing an electron above 100 MeV is 10^{-13}. These electrons are all less than 102 MeV (mostly near 100 MeV), and thus its measured energy must exceed 103.9 MeV by total mistake for the electron to be considered as fake signal. They have about 100 of signal to noise ratio at a sensitivity of 10^{-16}. In the PRIME experiment, there will be additional reduction of the background to the MECO since the energy gap between $E_{\mu e}$ and E^{emp}_{rmc} is more than 10 MeV, which is more than factor five larger than that of MECO. The measured energy of the electron must mistakenly exceed by more than 12 MeV, and which is very unlikely. The probability of the mis-measurement of the electron energy to the higher energy depends on the performance of the pattern recognition of the electron track. Detailed study by using

Monte Carlo simulation is under way. However, an additional reduction factor of a few orders of magnitude could be safely expected according to the study for the MECO experiment. As a result, the expected number of background events from the radiative muon capture at PRIME would be a level of 0.01 at a sensitivity of 10^{-18}.

7.4 Radiative Pion Capture

The radiative pion capture (RPC), $\pi^- + (A, Z) \rightarrow (A, Z-1) + \gamma$, followed by internal and external asymmetric e^+e^- conversion of the photon ($\gamma \rightarrow e^+e^-$) could be the most serious source of the background. Indeed, this background event appeared in the SINDRUM-II above the signal region. The probability of the photon emission is about 2% of the capture, and the photon energy spectrum has a peak at 110 MeV and endpoint at 140 MeV. The probability of photon conversion with a conversion electron in a signal window depends on the target material, thickness and the width of the signal window. By employing the estimation done for the MECO experiment, and taking into account the differences between MECO and PRIME, the probability is about 2×10^{-5}. In the PRIME experiment, all the charge particles are forced to travel about 150 m in the PRISM-FFAG ring. Since the $\beta\gamma\tau c$ of pions is at around 4 m, only a fraction of 3×10^{-17} of pions will survive and enters to the PRIME detector. The number of pions produced by a single 50 GeV/c proton is about 0.3 in the PRISM-FFAG momentum acceptance as calculated by a MARS simulation, and 10% of those pions will survive and enter to the FFAG. Thus, the expected number of this background events will be $[0.3] \times [0.1] \times [2 \times 10^{-5}] \times [3 \times 10^{-17}] = 2 \times 10^{-23}$ at most per 50 GeV proton on the production target. This corresponds to 0.03 events at the sensitivity of 10^{-18}.

7.5 Scattering of Beam Electrons

If the electrons whose energy at around 100 MeV enter the detector, they may scattered off the muon stopping target and may acquire the large p_t sufficient to be detected by the trackers. The sources of these electrons can be classified into (1) muon/pion decay in the pion decay section, (2) muon/pion decay in the PRISM-FFAG ring. In both cases, the electrons should have a momentum in the signal region ($\sim$ 104 MeV), and must be scattered off by the muon stopping target to acquire sufficient p_t to be detected.

As for the first category, the electron production rate in the pion decay section is about 2×10^{-5} per proton from Monte Carlo simulation. About 50% of them have an energy greater than 90 MeV. In addition, these electrons must go through in the PRISM-FFAG ring for 5 turns, while the momentum acceptance of the PRISM-FFAG ring is only less than 85 MeV/c. According to Monte Carlo simulations of the PRISM-FFAG ring, the electrons of 100 MeV which are injected into the PRISM-FFAG ring go only a half turn at most. The probability of such electrons surviving in the FFAG ring for a half turn is less than about 5×10^{-6}. This number is limited by the Monte Carlo statistics. Thus, the probability of the 100 MeV electrons go thorough in the PRISM-FFAG ring 5 turns would be a level of 10^{-53}. By combining all the numbers above, the expected event rate of an electron scattering background per a year (10^7 seconds) would be $[10^{14}] \times [1^7] \times [2 \times 10^{-5}] \times 50\% \times [10^{-53}] = 10^{-37}$, thus negligibly small. It should be noted that since beam electrons in the PRISM-FFAG ring have a different speed, the phase of RF would be totally random for the electron. The probability of the lower energy electrons stored in the ring being accelerated to the 100 MeV is negligible.

As for the second background category, the parent muon momentum should be larger than 77 MeV/c in order for the daughter electron to have energy above 102 MeV. The highest momentum of the muons injected into the FFAG ring is 85 MeV/c and it will be quickly reduced less than 77 MeV/c in the first 2.5 turns by phase rotation. Thus the electrons of 100 MeV must survive the rest of 2.5 turns in the ring to become a background. That probability is only a level of 10^{-27}. The fraction of muons decaying into electrons in the first 2.5 turns of the FFAG ring is about 20% of muons. Thus, the expected number of electrons with energy larger than 100 MeV per muon would be only a level of $20\% \times 10^{-27} = 10^{-28}$. In addition, at PRISM, when a beam is extracted from the PRISM-FFAG ring, a momentum selection[2] of about 68 MeV/c ($\pm 2\%$) can be placed to eliminate beam electrons further.

After all, the expected number of electron scattering events is totally negligible.

7.6 Muon Decay in Flight

Muons decaying in their flight can produce energetic electrons that mimic the true events if they are scattered at the muon-stopping target. In order for the electron to have energy above 102 MeV, the muon momentum must exceed 77 MeV/c. The case when the muon decay in the FFAG ring was already discussed in the previous section, here we discuss about the case when the muons decay after the FFAG ring. The muon momentum after the extracted from the FFAG ring is only 68 ± 2 MeV/c, and well blow 77 MeV/c. Thus, this background will be negligible.

7.7 Pion Decay in Flight

As was already discussed in the previous section, the pions survived and exited from the FFAG ring is only a level of 1.5×10^{-18} per 50 GeV proton on the production target. According to the study for MECO experiment, the probability of the decay electron to have energy more than 102 MeV and $p_t > 90$ MeV/c is about 5×10^{-6}. Thus the estimated number of background would be $[10^7] \times [10^{14}] \times [1.5 \times 10^{-18}] \times [5 \times 10^{-6}] = 0.008$.

[2] Some sort of momentum collimators can be placed at the exit of the PRISM-FFAG, where a beam might be dispersive.

7.8 Antiprotons

If an antiproton comes into the detector, it would annihilate and produce many photons, which in turn generate electrons and positrons. Therefore, antiprotons should be eliminated. In MECO, a proton energy will be lowered down to 8 GeV to suppress antiproton production. At the J-PARC 50-GeV PS, more antiprotons than in MECO would be produced at the production target. However, there are many ways to suppress antiprotons of low energy coming into the muon stopping target and the detector. They are (1) a backward take-off angle where lower production rate of antiprotons is expected, (2) a thin foil which could be placed inside the beam line at upstream to annihilate antiprotons, (3) a timing of kicking injection to PRISM-FFAG which eliminates slowly-drifting antiprotons and (4) momentum selection of antiprotons in the PRISM-FFAG ring. From those, antiproton rate should be reduced down to a sufficiently low level. Detailed evaluation of this background rate is now under way.

7.9 Cosmic Rays

Cosmic-ray induced electrons are potentially a serious background. In fact, in the past experiment (like SINDRUM-II), it has been reported that such background events were observed. The cosmic ray induced backgrounds can be reduced to a negligible level with a combination of active and passive cosmic ray shielding and detection of a extra particles in the tracking detector. They are almost the same as those adopted at MECO. Namely, (1) a passive shield of concrete (about 2 m) and steel (about 0.5 m), (2) two layers of scintillating veto counters surrounding the detector with high detection efficiency of charged particles, and (3) selection criteria to eliminate events having extra particles in either the tracking or calorimeter/trigger detectors in time with electron candidates. The MECO estimation of cosmic ray induced background is about 0.004 events per a 10^7 second run.

Since the same level of cosmic ray shielding is constructed at PRISM, the same background rate per unit time period as that at MECO can be expected. Therefore, the background rate can be scaled by a total integrated time of detection. Now, the beam repetition rate of PRISM is about 100 per 3 seconds (average 30 per seconds), whereas the MECO has about 370,000 beam pulses per seconds[3]. Therefore, if the same measurement time per a beam pulse is assumed, it is expected that the background rate at PRISM is a factor of 10,000 less than that of the MECO experiment. Therefore, the background rate at PRISM is about $< 4 \times 10^{-7}$ events per 10^7 seconds. It is almost negligible.

[3]one beam cycle consists of a 0.5 sec beam on with beam bunches of 1.35 μsec spacing and a 0.5 sec beam off)

7.10 Summary of Background Rates

Table 7.1 summarizes the expected background rate at PRIME for the sensitivity 10^{-18}. The most of the estimations were based on the study for MECO experiment. It is needless to mention that the PRIME dedicated study must be done. The study has just begun. However, the present estimations would still give sufficiently low levels of the backgrounds. It should be noted that the major feature of PRISM is to have sufficiently small background rates at a sensitivity of 10^{-18}, owing to the adoption of the PRISM-FFAG ring.

Table 7.1: A summary of estimated background rates at the sensitivity of 10^{-18}.

Background	Rate	Comments
Muon decay in orbit	0.05	
Radiative muon capture	0.01	
Radiative pion capture	0.03	
Beam electrons	negligible	see text
Muon decay in flight	negligible	see text
Pion decay in flight	0.008	
Anti-proton	negligible	see text
Cosmic rays	$< 10^{-7}$ events	
A total	0.10	

Chapter 8

Sensitivity

8.1 Acceptance

The net detection acceptance (A_μ) of our apparatus can be estimated to be about 0.22. The detailed breakup is shown in Table 8.1, where the analysis efficiency (such as the efficiency of electron tracking, the momentum cut of the signal region) is assumed to be 0.8.

In MECO, owing to slowly traveling pions in a beam, their time gate of measurement opens at a later time. In PRIME, no pion background (even slowly traveling ones) is expected. Thereby, the time gate of measurement can be opened from the time zero.

Table 8.1: A net acceptance of detection.

Items	values
Muon Stopping efficiency	0.8
Detector Geometrical Acceptance	0.35
Analysis Cut	0.8
A_μ total	0.22

8.2 Sensitivity

A single event sensitivity is given by a number of muons available and the detector acceptance. A single-event sensitivity[1] is given by,

$$B(\mu^- + A \rightarrow e^- + A) \sim \frac{1}{N_\mu \cdot A_\mu}, \tag{8.1}$$

where N_μ is a total number of muons and A_μ is acceptance of detection.

[1] A 90 % confidence level upper limit is given by $2.3/(N_\mu \cdot A_\mu)$.

8.2.1 Muon Yields from PRISM

As discussed in Chapter 5, the muon yield anticipated from PRISM depends on funding situation as well as the technology available at the time of PRISM construction. The most effective components are the pion production target, the pion capture field, and the PRISM-FFAG acceptance. Note that PRISM could be constantly kept upgraded to increase its muon beam intensity.

Various options and its corresponding muon yield are already shown in Table 5.2. To make evaluation of a sensitivity, two optional cases are chosen. One is an advanced case with the best performance, and the other is a feasible case with medium performance. The first case is to have a pion production target of heavy material, a pion capture field of 16 T, the PRISM-FFAG ring of the acceptance of 20,000 πmm·mrad in horizontal and 3,000 πmm·mrad in vertical. The second case is to have a graphite production target, a pion capture field of 8 T, the PRISM-FFAG ring of the acceptance of 20,000 πmm·mrad in horizontal and 3,000 πmm·mrad in vertical. Note that they are arbitrary choices selected as options. It should be stressed that since small background event rates is expected at PRIME as discussed in Chapter 7, the measurement could in principle run for a long term (like 5 years) until reaching the sensitivity where background events appear, as long as the running time is reasonable. This is one of the features of PRIME.

8.2.2 Sensitivity : Case 1

From Table 5.2, the first case gives $1.3 \times 10^{11}\mu^-$/sec. As mentioned, a long term running such as 5 years[2] is assumed. The single event sensitivity is

$$B(\mu^- + A \to e^- + A) \sim 6 \times 10^{-19}, \tag{8.2}$$

which is a factor of 30 better than the MECO goal of 2×10^{-17}. This single event sensitivity corresponds to a 90 % confidence level upper limit of about 10^{-18}.

$$B(\mu^- + A \to e^- + A) < 10^{-18} \quad (90\% \text{ C.L.}) \tag{8.3}$$

We like to note that PRIME will use a muon-stopping target of high Z material (higher than aluminum used in MECO). The use of a high Z target can become possible since the time gate of measurement can be opened from time-zero. In a high Z target, as shown in Figs.3.1, 3.2 and 3.3, a sensitivity to SUSY parameters is about twice better than in aluminum, even at the same signal sensitivity level.

8.2.3 Sensitivity : Case 2

From Table 5.2, the second case gives $3.0 \times 10^{10}\mu^-$/sec. After 5 year running, the single event sensitivity is

$$B(\mu^- + A \to e^- + A) \sim 3 \times 10^{-18} \tag{8.4}$$

which is a factor of 6 better than the MECO goal.

[2]One SSC year, namely 10^7 seconds per year is assumed. It is about 3000 hours

8.2.4 Sensitivity at J-PARC Phase II

The J-PARC Phase-II would have a 4.4 MW beam power. The single event sensitivity would be improved by a factor of about four more. To accomplish such a good sensitivity, the background rejection has to be further improved, because the background event rate is about 0.24 at the sensitivity of 10^{-18}, as discussed in Chapter 7.

Chapter 9

Conclusion

We, the PRIME (PRISM Mu E) working group, would like to express our interest to initiate a search for the $\mu^- - e^-$ conversion process in a muonic atom towards an ultimate sensitivity of 10^{-18}. Lepton flavor violation, in particular in the muon system, is one of the most important subjects in particle physics. It has a large discovery potential to find new physics beyond the Standard Model. Especially, it is sensitive to supersymmetric extension to the Standard Model. The sensitivity proposed would cover the most of parameter spaces in supersymmetric grand unification models and the minimal standard model with right-handed Majorana neutrinos.

To carry out the search for $\mu^- - e^-$ conversion process, where a single electron of the energy of 104.3 MeV is detected, the quality of muon beam is the most important. Thus we have proposed to construct a high intensity low-energy muon source called PRISM (= Phase Rotated Intense Slow Muon source). It has a narrow energy spread and no pion contamination. These features are of the critical importance. The letter of intent on PRISM has been submitted separately. We confidently show that the search for $\mu^- - e^-$ conversion process at a sensitivity of 10^{-18} with small background rates can be accomplished. We are also confident that a great discovery can be made with PRIME.

Bibliography

[1] Kuno Y and Okada Y, Review of Modern Physics, **73** (2001) 151.

[2] Hincks E P and Pontecorvo B 1947 *Phys. Rev. Lett.* **73** 246

[3] Brooks M L *et al.* (MEGA Collaboration) 1999 *Phys. Rev. Lett.* **83** 1521–1524

[4] Bellgardt U *et al.* 1988 *Nucl. Phys.* B **229** 1

[5] Wintz P 1998 in *Proceedings of the First International Symposium on Lepton and Baryon Number Violation*, edited by H.V. Klapdor-Kleingrothaus and I.V. Krivosheina (Institute of Physics Publishing, Bristol and Philadelphia), p.534

[6] Willmann L *et al.* 1999 *Phys. Rev. Lett.* **82**, 49

[7] Edwards K W *et al.* (CLEO Collaboration) 1997 *Phys. Rev.* B **55**, R3919

[8] Bliss D W *et al.* 1998 *Phys. Rev.* D **57** 5903

[9] Krolak P *et al.* 1994 *Phys. Lett.* B **320**, 407.

[10] Ambrose D *et al.* (BNL E871 Collaboration) 1998 *Phys. Rev. Lett.* **81** 5734

[11] Lee A M *et al.* 1990 *Phys. Rev. Lett.* **64**, 165.

[12] Arisaka K *et al.* 1998 *Phys. Lett.* B **432**, 230.

[13] Akers R *et al.* (OPAL Collaboration) 1995 *Z. Phys.* C **67**, 555

[14] Abreu P *et al.* (DELPHI Collaboration) 1997 *Z. Phys.* C **73**, 243

[15] Hall L J, Kostelecky V A and Raby S 1986 *Nuclear Physics* B **267** 415–432

[16] Barbieri R, Hall L and Strumia A 1995 *Nuclear Physics* B **445** 219–251

[17] Hisano J, Moroi T, Tobe K, and Yamaguchi M 1997 *Phys. Lett.* B **391** 341–350; Erratum 1997 *Physics Letters* B **397** 357

[18] Hisano J, Moroi T, Tobe T, Yamaguchi M, and Yanagida T 1995 *Phys. Lett.* B **357** 576

[19] Hisano J, Nomura D, and Yanagida T 1998 *Physics Letters* B **437** 351

[20] Hisano J and Nomura D 1999 *Phys. Rev.* D **59** 116005

[21] Kosmas T S, Faessler A and Vergados J D 1997 *J. Phys. G* **23** 693–703 : Kosmas T S and Vargados J D 1996 *Phys. Rep.* **264** 251–266 : Shanker O 1979 *Physics Review* D **20** 1608–1615

[22] Czarnechi A, Marciano W J and Melnikov K 1998 *Coherent Muon-Electron Conversion in Muonic Atoms* Preprint BNL-HET-98/2, TTP 97-19, hep-ph/9801218

[23] Raidal M and Santamaria A 1998 *Phys. Lett.* B **421** 250–258

[24] Weinberg S and Feinberg G 1959 *Phys. Rev. Lett.* **3** 111; **3** 244(E)

[25] Marciano W J and Sanda A I 1977 *Phys. Rev. Lett.* **38** 1512

[26] Kitano R, Koike M and Okada Y 2002 *Detailed calculation of lepton flavor violating muon-electron conversion rate for various nuclei* Preprint KEK-TH-808, hep-ph/0203110

[27] Honecker W *et al.* (SINDRUM II Collaboration) 1996 *Phys. Rev. Lett.* **76** 200

[28] Bachman M *et al.* 1997, a research proposal to Brookhaven National Laboratory AGS "A Search for $\mu^- N \rightarrow e^- N$ with Sensitivity Below 10^{-16}, **M**uon – **E**lectron **CO**nversion"

[29] Dzhilkibaev R M and Lobashev V M 1989 *Sov. J. Nucl. Phys.* **49** 384

[30] Bryman D A, Blecher M, Gotow K and Powers R J 1972 *Phys. Rev. Lett.* **28** 1469

[31] Badertscher A *et al.* 1982 *Nucl. Phys.* A **377** 406

[32] Bryman D A *et al.* 1985 *Phys. Rev. Lett.* **55** 465

[33] Ahmad S *et al.* 1988 *Phys. Rev.* D **38** 2102

[34] Dohmen C *et al.* (SINDRUM II Collaboration) 1993 *Phys. Lett.* B **317** 631

[35] Barkov L M *et al.* 1999, a research proposal to PSI "Search for $\mu^+ \rightarrow e^+\gamma$ down to 10^{-14} branching ratio"

[36] Kuno Y *et al.* 1998 in *Proceedings of Workshop on High Intensity Secondary Beam with Phase Rotation* edited by Y. Kuno and N. Sasao p.71

[37] J.D. Jackson "Classical Electro Dynamics", third edition, John Wiley & Sons, Inc. (1998)

[38] Shanker O 1982 *Phys. Rev.* D **25** 1847

[39] Hänggi P, Viollier R D, Raff U nd Adler K 1974 *Phys. Lett.* **51B** 119

[40] Herzog F and Adler K 1980 *Helv. Phys. Acta* **53** 53

[41] Primakoff H 1959 *Rev. Mod. Phys.* **31** 802

[42] Armstrong D S *et al.* 1992 *Phys. Rev.* C **46** 1094

[43] Kaulard J *et al.* 1998 *Phys. Lett.* B **422** 334

Appendix A

R&D of Low-Mass Tracking Chambers

A.1 Introduction

The electron tracking detector is used to measure helical trajectories of electrons in a solenoidal magnetic field to distinguish the $\mu^- - e^-$ conversion electron from background electrons. Muon decay in orbit is one of the major background sources in the search for μ^--e^- conversion in a muonic atom since the end point of the electron spectrum comes close to the signal region of the $\mu^- - e^-$ conversion. In Fig.7.1 in Section 7.2, the effective branching ratio of the muon decay in orbit is shown as a function of electron energy for the case of a titanium target, where the conversion electron energy is 104.3 MeV. In order to distinguish the conversion electrons from backgrounds, the tracker must have a 350 keV resolution (FWHM) for PRIME.

Since the energy of the electrons from μ-e conversion is as low as 104.3 MeV, the intrinsic momentum resolution is dominated by multiple scattering in the tracker materials. Because of this, the reduction of the mass of the trackers and the installation in a vacuum environment are of great importance. In order to meet the above requirements, we chose straw gas chambers as the tracking detectors for PRIME.

The hit positions in the radial direction are determined by a drift time, and those in the axial direction can be determined by induced charges on the cathode strips placed on the exterior of the straw tubes. Figure A.1 illustrates a schematic configuration of the straw gas chambers. The requirements of position resolutions are 0.1 mm (r.m.s.) from a drift time measurement, and 1.4 mm (r.m.s.) from a cathode readout. These requirements are based on the Monte Carlo study for the MECO experiment. Since the net momentum resolution of the electron is dominated by energy loss in the muon stopping target, the same performance of the trackers as developed for MECO could be also sufficient for the PRIME experiment. The straw gas chambers have several advantages in comparison to other tracking detectors, such as multiwire proportional chambers. In particular, the straw gas chambers with cathode pads have the advantages listed below.

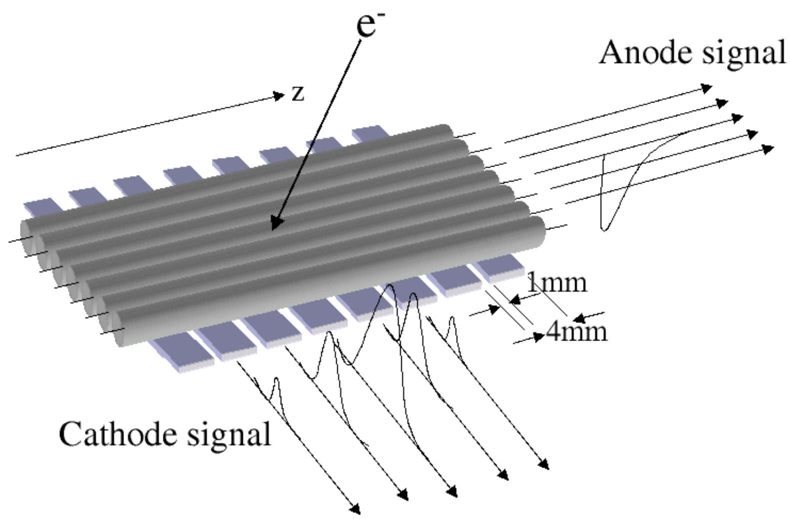

Figure A.1: The principle for reading the signals from the straw gas chamber.

- The cylindrical shape makes it possible to stand for a pressure from the gas inside, even with its very thin wall (25 μm). This reduces a total mass of the chamber and thus decreases an effect of multiple scatterings, while keeping a large effective area of detection.
- From the same reason, straw gas chambers have an excellent ability to operate in vacuum without explosion of the chamber wall.
- The position resolution obtained by the cathod readout along the axial direction is much better than the other readout methods such as a charge division method and a delay line method.
- It may be possible to use the timing information of the cathode readout to measure a drift time. By doing this, a single tube may be able to measure each drift time for multiple hits at the same time. This increases a total performance of the multi-tube chamber system under a very high counting rate.

A.2 Beam Test of Prototype Chamber at KEK PS

We have constructed a prototype straw gas chamber with 31 straws. Its picture is shown in Fig. A.2. It consisted of 20 resistive straw tubes in the first and the third layers, and 11 conductive one in the middle layer. The dimensions of the straw tubes were 25 μm in thickness, 5 mm in diameter and 35 cm in length. Their resistance of the resistive straw tubes is about 6 M$\Omega/\Box$.

In order to study the performance of the chamber, a beam test was done at the $\pi 2$ beam line in the east counter hall of KEK 12GeV PS. A gas mixture was chosen to

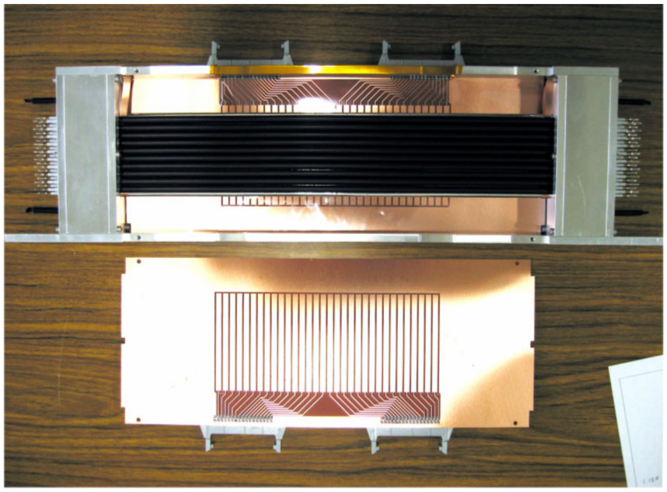

Figure A.2: Photograph of the prototype chamber.

be Ar(50%)-C_2H_6(50 %). A high voltage applied to the anode wire was 1.65 kV. The amplifier shaper discriminator (ASD), which was developed at KEK for the thin gap chambers of the ATLAS experiment, was employed as a readout for both the cathode and anode signals. The ASD provides both the discriminated digital signal as well as the amplified analog signal. Figure A.3 shows both the anode and the cathode signals from the ASD.

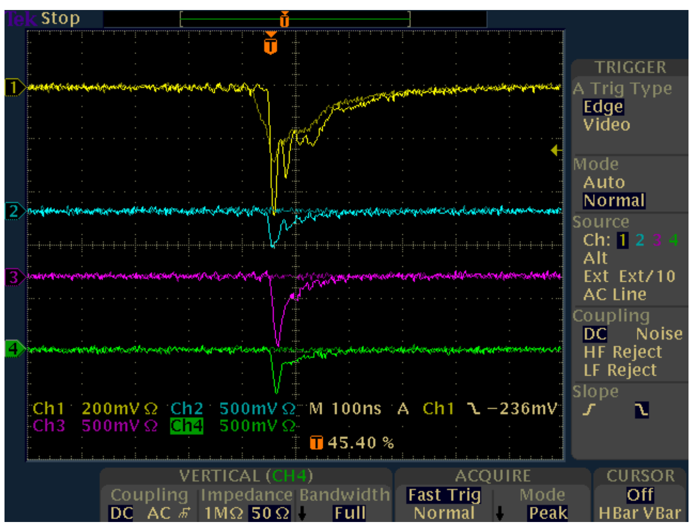

Figure A.3: Analog signal from the ASD chip for 55-Fe X-ray sources. The top signal is from the anode, the third signal from the top is from the central cathod strip, where the X ray source was placed. The second and forth signals from the top are its adjacent cathod strips.

The beam test was performed with different orientations of the straw gas chambers to the beam in order to evaluate the incident angle dependence of the chamber resolution for both the anode and cathode measurement. The definition of the incident angles, ϕ and θ, is shown in Figure A.4.

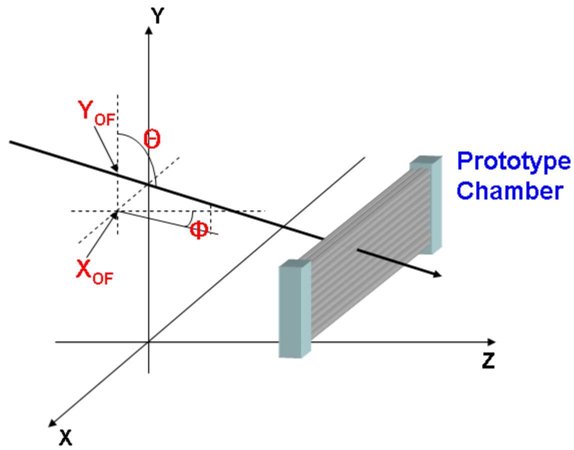

Figure A.4: The definition of the incident angles

A.2.1 Cathod Measurements

Figure A.5(a) shows the position resolution of the prototype chamber along the axial direction. The ϕ-angle dependence of the resolution is shown in Figure A.5(b). The resolution becomes worse as the ϕ-angle increases. It could be understood since a length of avalanche along the anode wire increases as the ϕ-angle increases. A longer avalanche along the anode may make the charge distribution induced at the cathode pads much wider, thus resulting in a worse position resolution.

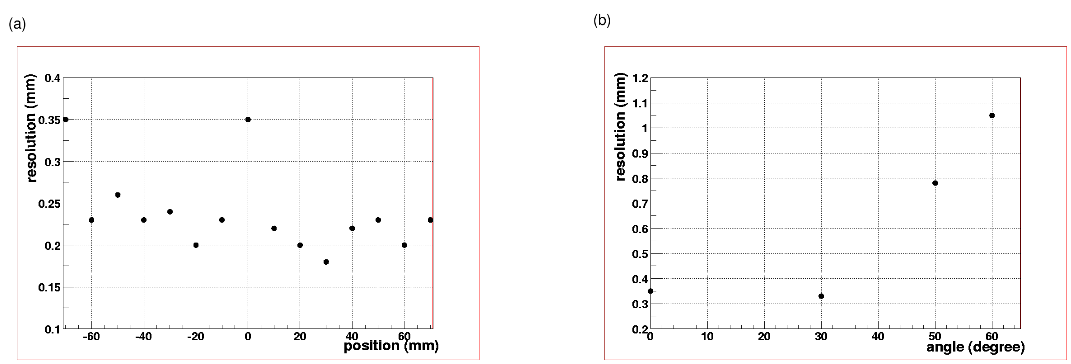

Figure A.5: (a) Resolution of the prototype chamber along the axial direction of the straw tubes, and (b) ϕ-angles dependence of the resolution.

Figure A.6(a) shows the chamber efficiency as a function of hit position along the perpendicular direction to the anode wire. The efficiency drop was observed at around the boundary of adjacent tubes. This is because of a path length of charged particles inside the tube becomes shorter. A shorter path length results in a less number of initial ions, and thus a smaller signal. Note that this is a special case for the perpendicular track, in which the track can path through the boundary of the tubes without leaving any ions in either tube. This is not the case for tilted angle tracks, such as $\theta = 30°$, for example. Fig. A.6(b) shows an efficiency for tracks of $\theta = 30°$. The efficiencies were thus recovered.

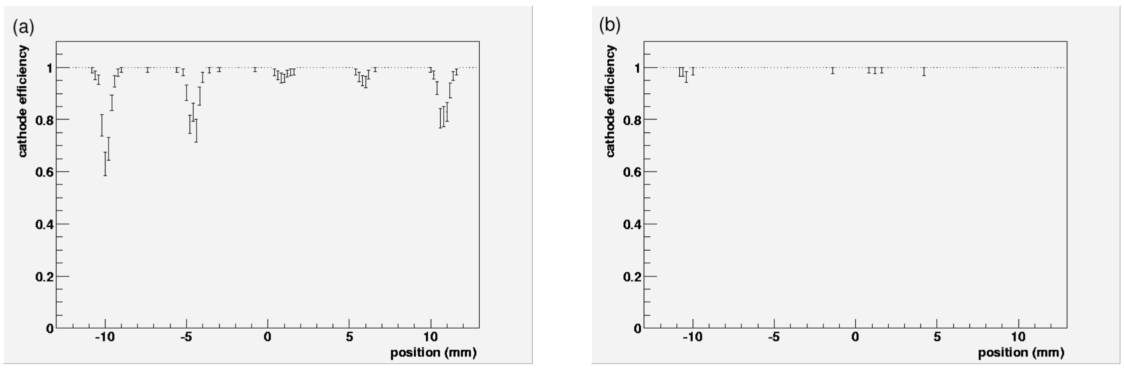

Figure A.6: θ-angle dependence of chamber efficiency for the cathode readout. (a) $\theta = 0°$, (b) $\theta = 30°$.

A.2.2 Anode Measurements

The measurement of drift times is accomplished by reading a time of the anode signal. The drift time is then translated into a corresponding drift length. Then, a straight line was fit to a group of drift circles in order to obtain a most probable trajectory of the incident particle. The resolution of each drift circle was extracted from the stretch function of fitting. Figure A.7 shows the spacial resolution of drift circles as a function of ϕ-angle of the track. The resolution becomes much better as the ϕ-angle increases. This is simply because of an initial number of the ions increases as the ϕ-angle increases.

For the same reason, as was discussed previously for the cathode readout, the efficiency of the anode readout for the tracks near the walls is low. However, it was restored for tracks with finite angles. These are shown in Figure A.8.

A.2.3 Conclusion

The straw gas chamber is an ideal tracker for PRIME. We have manufactured a prototype chamber by using resistive seamless straws. And we have tested the performance at KEK with a 1 GeV/c pion beam. The observed resolution was 250 μm from the

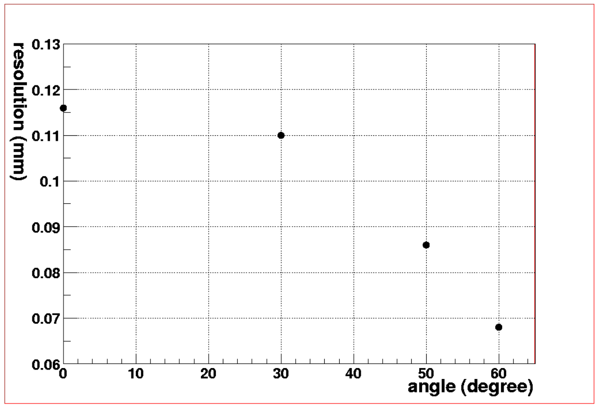

Figure A.7: Resolution of drift circle as a function of ϕ-angle.

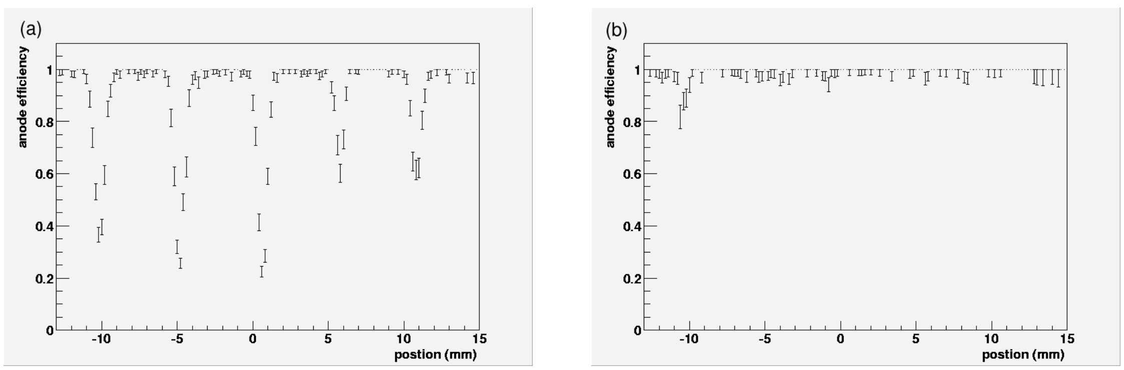

Figure A.8: θ-angle dependence of efficiency for anode readout. (a)$\theta = 0°$, (b)$\theta = 30°$.

cathode readout, and 100 μm from the anode readout for $\theta = 0°$ incident tracks. The resolution of the cathode strips becomes worse as the ϕ-angle increases, while the resolution of the anode readout becomes better as the ϕ-angle increases. The efficiencies of both the anode and cathode readouts were almost 100 %, except for the boundary of the adjacent straw tubes. This efficiency was restored if the θ-angle of the incident particles increases. The resolutions and the efficiency we obtained from the beam test meet the requirements for PRIME.

A.3 Things To Be Done

The R&D activity for the straw gas chambers is still on-going. The issues that we are going to study are listed below.
(1) A test in a high rate environment

(2) Optimization of the gas mixture
(3) Proof of the operation in vacuum
(4) Improvement of the design of readout circuit
(5) Design of the real chambers